

Copyright is owned by the Author of the thesis. Permission is given for a copy to be downloaded by an individual for the purpose of research and private study only. The thesis may not be reproduced elsewhere without the permission of the Author.

Design and analysis of a novel piezoelectric rotary motor
with the cyclic symmetric stator

Master of Engineering
In
Mechatronics

By

Hong-Yi Cheng

School of Engineering and Advanced Technology
Massey University
New Zealand
2011

Abstract

Piezoelectric motors have been widely employed since 1980s when the first commercial model was invented. Various types of ultrasonic motors have been constructed and manufactured. The piezoelectric motors have been noticed in the last few decades in the field of autofocus cameras, miniature robotics and car applications due to the significant mechanical characteristics such as light-weight, simplicity of design and compact. The aim of this study is to design and analyze a novel piezoelectric rotary motor with the cyclic symmetric stator. Hence, a novel cyclic symmetric stator design with evenly-spaced protrusion fingers was developed. The natural frequencies and mode structures of the cyclic symmetric stator was examined by using the finite element method. The deformation relationship between stator disk and protrusion fingers in repeat and split modes will be discussed in this article. Furthermore, this modeling study focused more on displacement strength and deforming direction of the protrusion fingertips using the Fourier coefficients. The piezoelectric buzzer was attached to the cyclic symmetric stator prototype for driving the stator's natural frequencies. An experimental prototype is built to examine the consistency with the simulation results.

Acknowledgement

Studying toward to Master degree in Massey has been the most important and extraordinary experience in my life. This training progress has improved the way of my thinking and ability of solving problems.

I would like to thank my thesis adviser Dr. Jen-Yuan (James) Chang whose expertise, advice and continuous support during the research. I consider myself extremely fortunate to work under his supervision.

I would also like to thank Dr. Johan Potgieter, Eddie Rogers, Paul Thornton and Joe Wang for the manufacturing support. Also, I felt gratitude to the faculty staff for their help and Massey University staff for their various support during the study.

I am further indebted to current and past colleagues (Rana Noman Mubarak, Amur Alminji, Hamid Reza Memarbashi, Riichi Nagao, Ivan Ernesto Cortes Zambrano, Di Wu and Jason Li) in my research lab for their valuable feedback and knowledge.

Finally, I would like to express my appreciation to my parents and other family members who have provided continuous encouragement and support to all my educational pursuits. They have helped me go through the challenges along the way. I certainly wouldn't have made it this far without them.

Table of Contents

Chapter 1 Introduction.....	1-1
1.1. Piezoelectric Motor.....	1-1
1.2. Applications.....	1-2
1.3. Scope and contribution	1-10
1.4. Thesis Outline	1-10
Chapter 2 Fundamental of piezoelectricity theory	2-1
2.1. Chapter Overview	2-1
2.2. The phenomenon of piezoelectricity.....	2-1
2.3. Piezoelectric Materials	2-3
2.4. Piezoelectric Actuator	2-6
Chapter 3 System configuration	3-1
3.1. Chapter Overview	3-1
3.2. Model Description	3-1
3.2.1. Rotor.....	3-3
3.2.2. Stator	3-3
3.2.3. Piezoelectric ceramic buzzer	3-5
3.2.4. Base.....	3-5
3.3. Finite Element Analysis.....	3-5
3.4. Chapter summary.....	3-12
Chapter 4 Parametric study of cyclic symmetric stator.....	4-1
4.1. Chapter Overview	4-1
4.2. Parametric study	4-1
4.2.1. Displacement variation with varying contact angle	4-2
4.2.2. In-plane deformation angle with varying contact angle	4-8
4.3. Chapter summary.....	4-13
Chapter 5 Experimental result.....	5-1
5.1. Experimental setup	5-1
5.2. Experimental result	5-3
5.3. Chapter summary.....	5-6

Chapter 6 Summary 6-1

6.1. Structure response in a novel cyclic symmetric stator model 6-1

6.2. Displacement strength and in-plane deformation angle of the cyclic symmetric stator 6-2

6.3. Limitations 6-2

6.4. Directions for future work 6-3

Reference R-1

Appendix A-1

List of Figures

Figure 1: Fundamental construction of Barth motor (1: rotor, 2: shaft, 3: active element, 4: piezoelectric plate)	1-3
Figure 2: (a) Piezo Systems Ultrasonic Motor (Shinsei USR30) and (b) Traveling Wave Formation	1-5
Figure 3: Auditory tele-existence robot TeleHead	1-7
Figure 4: Mechanism of TeleHead II	1-7
Figure 5: Design of multi-DOF surgical instrument.....	1-8
Figure 6: Master–slave system for surgical instrument	1-9
Figure 7: Direct Piezoelectric Effect	2-2
Figure 8: Converse Piezoelectric Effect	2-2
Figure 9: Perovskite structure	2-3
Figure 10: Polarization of crystals	2-4
Figure 11: Polarization of the piezoelectric ceramic domains.....	2-5
Figure 12: The polling process	2-5
Figure 13: Schematic view of a piezoelectric buzzer.....	2-6
Figure 14: Structure of the piezoelectric rotary motor.....	3-2
Figure 15: schematic of the cyclic symmetric stator	3-4
Figure 16: Mesh of the cyclic symmetric stator model with boundary condition	3-6
Figure 17: Simulation result from Solidworks (Mode Shape 1~5).....	3-8
Figure 18: Simulation result from Solidworks (Mode Shape 6~10).....	3-9
Figure 19: Modified cyclic symmetric stator with 4 and 6 evenly-spaced protrusion fingers in P(0,2) and P(0,3) respectively	3-11
Figure 20: Contact angle at 0° - (a) nodal patterns and (b) the displacement strength of protrusion fingertips. (c) the corresponding Fourier coefficients.....	4-3
Figure 21: Contact angle at 30° - (a) nodal patterns and (b) the displacement strength of protrusion fingertips. (c) the corresponding Fourier coefficients.....	4-4
Figure 22: Contact angle at 45° - (a) nodal patterns and (b) the displacement strength of protrusion fingertips. (c) the corresponding Fourier coefficients.....	4-5

Figure 23: Contact angle at 60° - (a) nodal patterns and (b) the displacement strength of protrusion fingertips. (c) the corresponding Fourier coefficients	4-6
Figure 24: Contact angle at 0° - Protrusion fingertips deformed angle in (a) sine and (b) cosine oriented components	4-10
Figure 25: Contact angle at 30° - Protrusion fingertips deformed angle in (a) sine and (b) cosine oriented components	4-11
Figure 26: Contact angle at 60° - Protrusion fingertips deformed angle in (a) sine and (b) cosine oriented components	4-12
Figure 27: Piezoelectric rotary motor experimental setup	5-2
Figure 28: Chlandi-type measurement used on the cyclic symmetric stator.....	5-4
Figure 29: Rotation performance.....	5-5
Figure 30: 0° disk edge displacement and corresponding harmonic.....	A-6
Figure 31: 15° disk edge displacement and corresponding harmonic.....	A-7
Figure 32: 30° disk edge displacement and corresponding harmonic.....	A-8
Figure 33: 45° disk edge displacement and corresponding harmonic.....	A-9
Figure 34: 60° disk edge displacement and corresponding harmonic.....	A-10
Figure 35: 0° finger base displacement and corresponding harmonic.....	A-11
Figure 36: 15° finger base displacement and corresponding harmonic.....	A-12
Figure 37: 30° finger base displacement and corresponding harmonic.....	A-13
Figure 38: 45° finger base displacement and corresponding harmonic.....	A-14
Figure 39: 60° finger base displacement and corresponding harmonic.....	A-15

Chapter 1

Introduction

1.1. Piezoelectric Motor

Nowadays, the size minimization of electrical drives used in small-scale actuation has become an important design issue. Several applications, such as micro-satellite, micro-robot actuation and servo-drives used in the field, require operation at high torque and low speed. Most electric drives use electromagnetic motors due to the operation principles are well understood and the designs are optimized for a variety of applications. High torque at low speed is achieved by using a gear reduction unit, which leads to an increase in the size and mass of the drive. Electromagnetic motors use a magnetic field to generate torque; however, these motors cannot operate if a strong external magnetic field is presented, as their rotor will lock on the direction of the external magnetic field. The electromagnetic motor is limited in this aspect without new findings on new designs or materials. Therefore, the attention of researchers and engineers turned to a new type of motor – “piezoelectric motor.”

The piezoelectric motor became well-known and appeared in high numbers in commercial products since 1980s, and opened a new horizon in the field of small electric drives due to specific advantages, this type of motor possesses over the classical electromagnetic motor. Piezoelectric motors are also known as ultrasonic motors. The term of “ultrasonic” is for the reason that the drive frequencies of these motors are in the range of 25 to 70 kHz. The main characteristics and advantages of this type of motor are:

- a high torque at low speed without using a gear [1]
- a simple redesign by providing additional piezoelectric material mounted on the same stator
- the ability to operate in a vacuum
- the ability to operate in strong magnetic fields
- silent operation due to the fact that the excitation signals are at ultrasonic frequencies
- a simpler construction than electromagnetic motors and simple manufacturing process

Ultrasonic motors have widest range of applications. For example, It has been used in the automotive industry for headrest and seat adjustment, for the rotational scanning mount of a television camera, for auto focusing in Canon cameras and last but not least for micro-robot actuators [2]-[3].

1.2. Applications

There are several successful applications and research prototypes around the world of piezoelectric motors. Some applications, research and prototypes will be reviewed in the following paragraphs.

The earliest attempt of ultrasonic motor (as shown in Figure 1) was proposed by H V Barth of IBM in 1973 [4]. The rotor was loaded against two horns placed at different locations. By exciting one of the horns, the rotor was driven in one direction, and by exciting the other horn, the rotation direction was reversed. Based on the same principle, many mechanisms were proposed [5]-[6]. However, the motors were not of many practical uses at that time due to the difficulty in maintaining constant vibration amplitude with temperature rise, wear and tear.

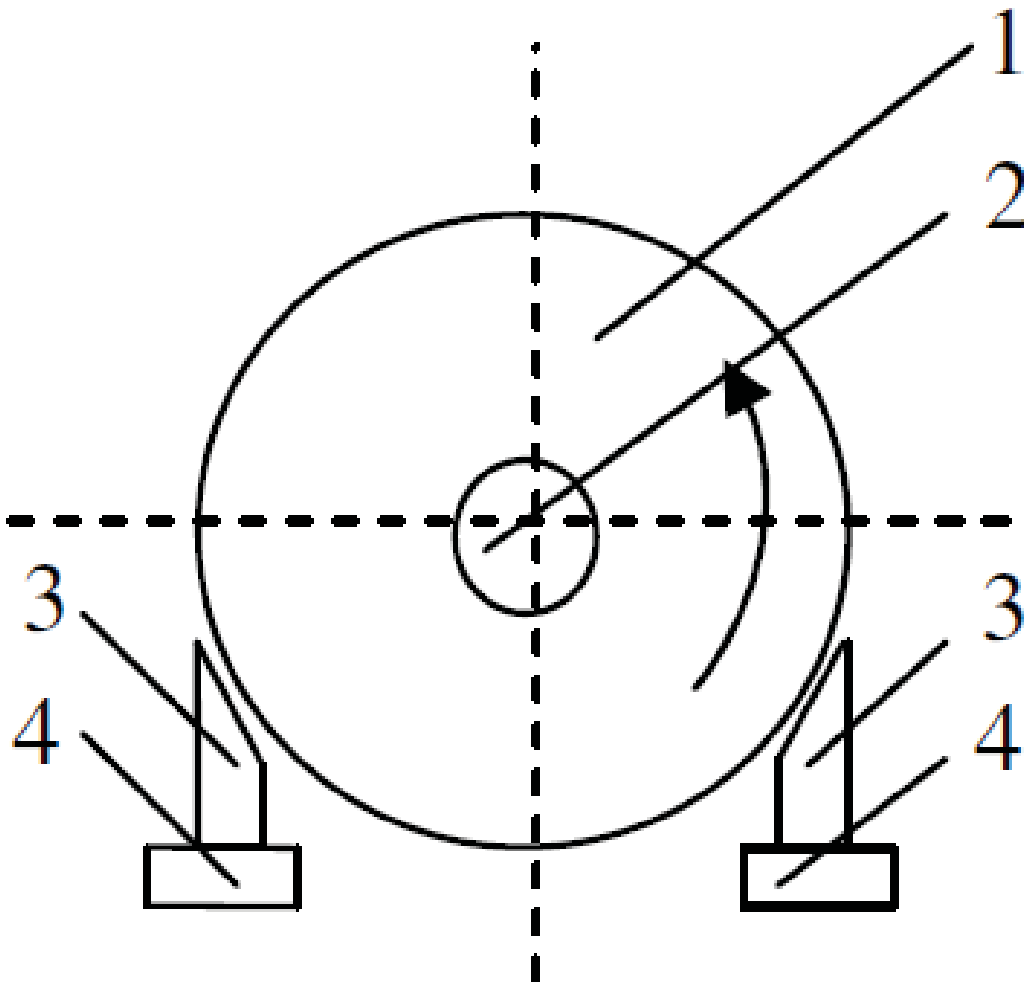


Figure 1: Fundamental construction of Barth motor (1: rotor, 2: shaft, 3: active element, 4: piezoelectric plate)

Later on, Sashida designed and made a standing wave ultrasonic motor which used a Langevin vibrator. The driving frequency of this motor was 27.8 kHz with input electric power of 90W, output mechanical power of 50W, output torque of 0.5N·m, output rotational speed of 2800 rpm/min, and the efficiency was 60%. This motor's metal film and the rotor were fixed at the same position and serious wears existed on the contact surfaces. It was believed that this piezoelectric ultrasonic motor met the performance requirements for actual applications at the first time.

In 1982, the mechanism, the traveling-wave ultrasonic motor [1] (TWUSM) was invented by Toshiiku Sashida of Shinsei Co. Ltd. of Japan. This model has improved the problem of wear between the stator and the rotor- and Shinsei licensed the ensuring patent to Canon. Thus, in 1985, Canon introduced the ring USM drive on its EF 300 mm f/2.8L USM lens established on the ultrasonic motor technology. This ultrasonic motor became the first commercial ultrasonic motor. In addition to the use of the principle in lenses, Canon also offered a wide line of ultrasonic motors for industrial, scientific, and consumer goods applications. Since ultrasonic motors developed by Sashida were commercialized, this new concept motor aroused the interest of engineers and researchers. Various ultrasonic motors with different exciting principles, structures and performances have been developed [7]-[11]. On the basis of the vibration mode, ultrasonic motors can be categorized into either standing wave ultrasonic motor or travelling wave ultrasonic motor. The detailed examples of these two types of ultrasonic motor will be introduced in the following section:

A typical piezoelectric ultrasonic motor (Shinsei USR 30) as depicted in Figure 2 , consists of a toothed piezoelectric disk (stator) in contact with a metal disk (rotor). Time-varying electric fields applied to the piezoelectric stator inducing a travelling wave which is mechanically rectified; causing the rotor to rotate. This mechanism produces relatively high torque at low rotor angular velocities and obviates the need for gearing. The friction between rotor and stator provides a passive holding torque typically larger than the rotating torque and eliminates the need for mechanical brakes or active holding torque.



(a)

(b)

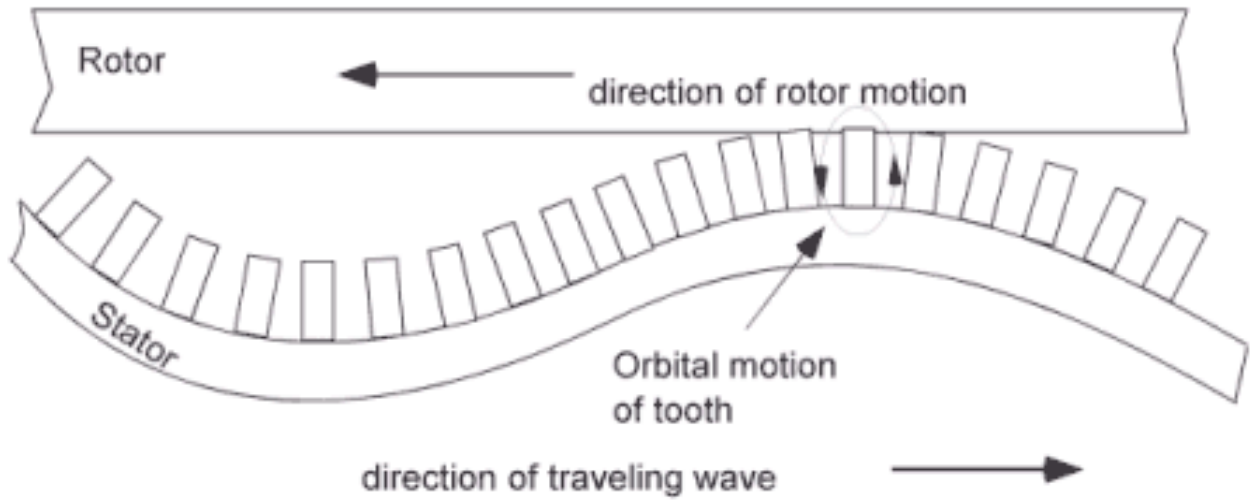


Figure 2: (a) Piezo Systems Ultrasonic Motor (Shinsei USR30) and (b) Traveling Wave Formation

These motors can be built without producing or being affected by magnetic fields, making them useful in highly magnetic environments and applications in which magnetic fields are harmful. Nevertheless, the state of the art in control of piezoelectric ultrasonic motors (PUM) is not fully developed. Commercial motors typically employ open-loop speed controllers which are operated in cascade with non-model-based control schemes such as proportional-integral-derivative control. These techniques are effective and appropriate for many applications for example, the locomotion. Also, the techniques are not suitable for precise positioning, or for mission-critical applications requiring guaranteed stability and performance characteristics. The goal of PUM research conducted in the University of Houston – Clear Lake (UHCL) Systems Engineering Laboratory is to develop model-based real-time control algorithms for PUM. Supportive research of ISSO entailed characterizing the kinematic performance of a commercial variable-frequency motor driver and designing a custom driver that provides greater variations in driving signal frequency as well as variable driving signal amplitude.

TeleHead [12] is a prototype of ultrasonic motor application which is developed as a test bed of a new sophisticated telecommunications tools. By introducing tele-existence technology, the TeleHead can transmit real sound fields of a remote place to the user, giving the user a feeling of being at a remote place. The “TeleHead I” (Figure 3) and “TeleHead II” (Figure 4) was built in 2001 and 2003 respectively. TeleHead has a dummy head that has the same head-related transfer function (HRTF) as the head of its remote user. Remote users can localize the sound source by listening to the sound received by microphones installed in the dummy head. The dummy head tracks the head motion of the user in real time by means of a 3-degree-of-freedom (DOF) control mechanism that uses two electrical AC servomotors for pitch and roll, and a DC direct-drive servomotor for yaw.



Figure 3: Auditory tele-existence robot TeleHead

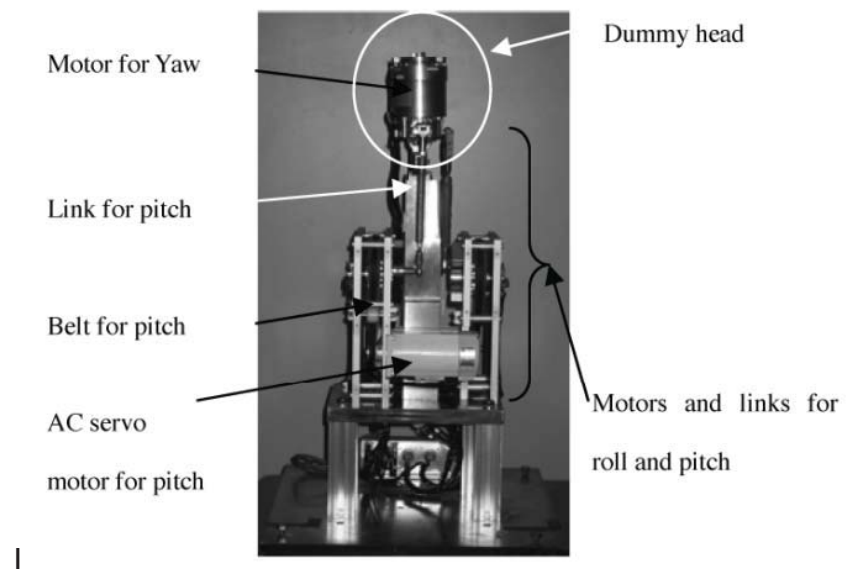


Figure 4: Mechanism of TeleHead II

Another novel ultrasonic motor prototype [13] is introduced to control three-degree-of-freedom (DOF) rotational motion, by enabling spin motion at the wrist. The actuated wrist joint controls pitch, yaw and spin motions of the forceps, where the pitch motion is the rotation along y-axis, the yaw motion along x-axis, and the spin motion along the centerline of gripper (Figure 5).

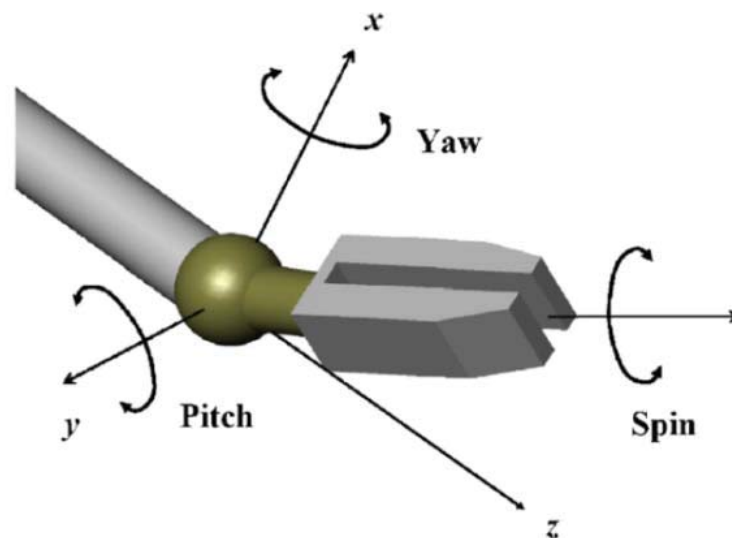


Figure 5: Design of multi-DOF surgical instrument

In addition to the four-DOF global motion at the pivot point, three extra DOF (spin, pitch and yaw) are implemented in the wrist to enable more precise and dexterous surgical operations: pitch and yaw motions are useful in accessing the surgical site, and spin motion enables suturing and knotting procedures. Figure 6(a) shows a master–slave

system we have constructed based on the design described above. A thumb-controlled joystick serves as the master port (Figure 6(b)), and the forceps with the actuated wrist constitutes the slave port (Figure 6(c)).

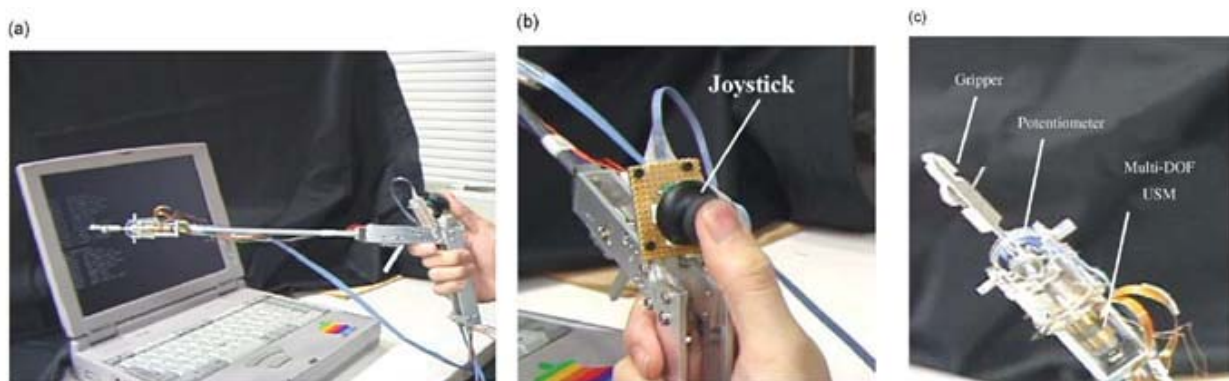


Figure 6: Master–slave system for surgical instrument

All the mentioned product and prototypes of ultrasonic motor is excited by piezoelectric elements in ultrasonic frequency range which develop different kinds of vibrations depending on its structure. From the way of creating an elliptical motion on the stator, ultrasonic motors can be classified into two major groups, which are standing wave and traveling wave types. The ultrasonic motors are of great interest due to the flexibility of miniaturization in comparison with conventional electromagnetic motors whose efficiency decreases significantly. Hence, the compact size of the motors makes engineers and researchers exploring wider applications particularly in the information technology and the medical industry.

1.3. Scope and contribution

Previous studies have focused on the piezoelectric stator. The stator is induced by travelling wave or combining two bending modes and a longitudinal mode of the actuators. The effects on the actuator's driving frequencies and mounting location on the stator have been thoroughly examined, however, there is very little literature concentrating on the structure response and motion behavior of the stator under different excitation of natural frequencies.

Hence, the objective of this thesis is to classify and characterize the response of the novel cyclic symmetric stator design in varied natural frequencies using experimental and analytical techniques. Once the frequency and mode structure are established, the behavior of the protrusion fingers on the designed stator can be examined. The contributions of the thesis are:

- A cyclic symmetric stator model was developed
- The natural frequency and mode shape structure was identified
- The structure response of the cyclic symmetric stator and protrusion finger was examined
- The displacement strength and in-plane bending distorted angle of the protrusion fingers in different rotor contact area was also examined

1.4. Thesis Outline

This thesis presents structure response under different natural frequencies in the novel cyclic symmetric stator design. A brief overview of this study will be provided in this section.

The fundamentals of piezoelectricity theory will be briefly discussed in Chapter 2 followed by the configuration of the experimental piezoelectric actuator.

In chapter 3, commercial software SolidWorks is used to design the structure of the piezoelectric rotary motor with proposed cyclic symmetric stator. The finite element method is employed to examine and characterize frequencies and mode shapes of the stator structure. Deformation of protrusion fingers and disk of the stator are examined on different natural frequencies and mode shapes.

In chapter 4, the measured data from simulation results is employed to investigate the displacement strength variation and deformation direction of the protrusion fingertips through Fourier expansion methods.

Chapter 5 discusses the experimental setup and the result of the novel piezoelectric rotary motor with cyclic symmetric stator.

Chapter 6 lists the conclusions based on the results obtained from this study. The study limitations, recommendations and future application directions are also included.

Chapter 2

Fundamental of piezoelectricity theory

2.1. Chapter Overview

In this thesis, the piezoelectric ceramic actuator was employed and mounted on the proposed stator. The basic phenomenon and characteristic of the piezoelectric material will be briefly introduced and the configuration of experimental piezoelectric buzzer will also be reviewed in the following section.

2.2. The phenomenon of piezoelectricity

The phenomenon of piezoelectricity was discovered in 1880 by Jacques and Pierre Curie during their study of the effects of pressure on the generation of electrical charge by crystals such as Quartz, tourmaline, and Rochelle salt. In 1881, the term "piezoelectricity" was first suggested by W. Hankel, and the converse effect was deduced by Lipmann from thermodynamics principles. The piezoelectric effect consists of the appearance of an electric potential across certain faces of some crystals when these crystals are subjected to mechanical stress. Tension and compression generate voltages of opposite polarity (shown in Figure 7), and in proportion to the applied force. The phenomenon is called the direct piezoelectric effect. In addition to the direct piezoelectric effect, it has been discovered that if one of these voltage-generating crystals was exposed to an electric field it lengthened or shortened according to the polarity of the field, and in proportion to the strength of the field (shown in Figure 8). This phenomenon is called the converse piezoelectric effect.

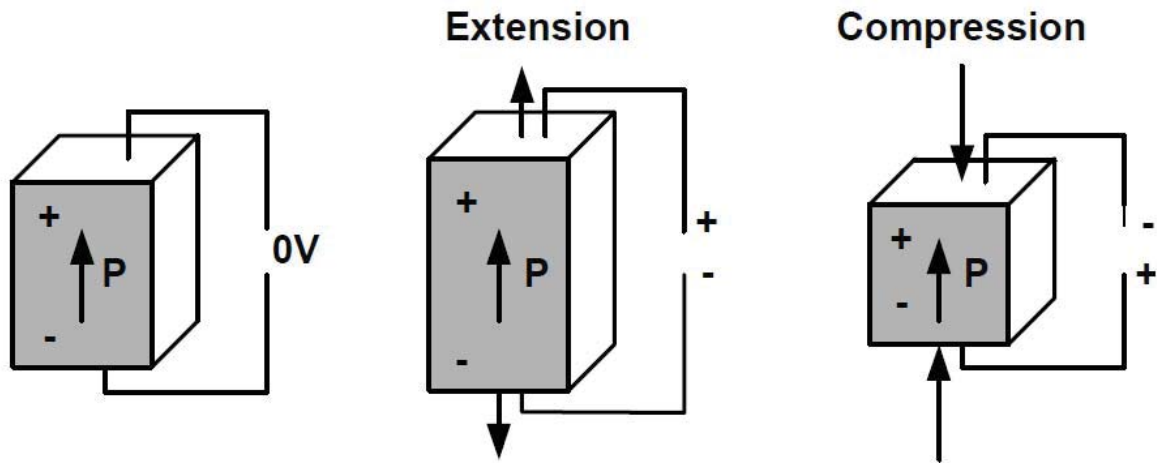


Figure 7: Direct Piezoelectric Effect

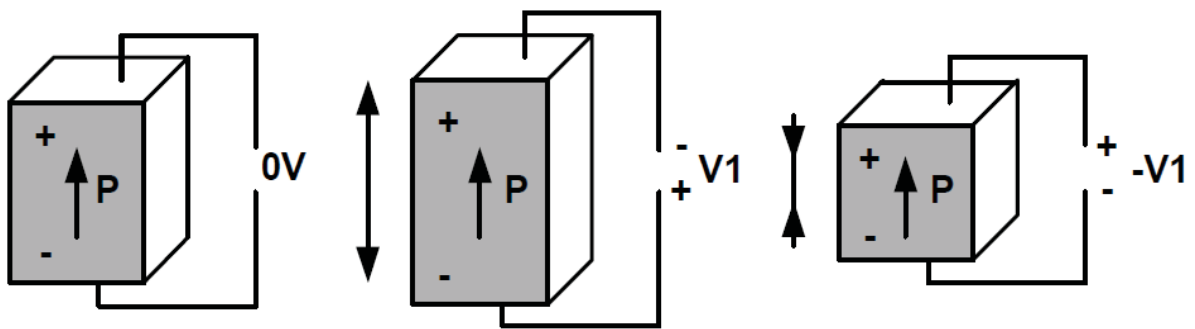


Figure 8: Converse Piezoelectric Effect

2.3. Piezoelectric Materials

The phenomenon of piezoelectricity appears in natural and synthetic crystals such as quartz, Rochelle salt, lithium sulphate; and ammonium dihydrogen phosphate, as well as in piezoceramic materials such as lead zirconate titanate (PZT), barium titanate, and cadmium sulphide. These materials usually have a perovskite structure such as the one shown in Figure 9 for a piezo-ceramic material. The perovskite structure exists in two crystallographic forms. Above the Curie temperature, the perovskite presents a cubic structure (shown in Figure 9a) and below the Curie temperature they transform into a tetragonal structure (shown in Figure 9b).

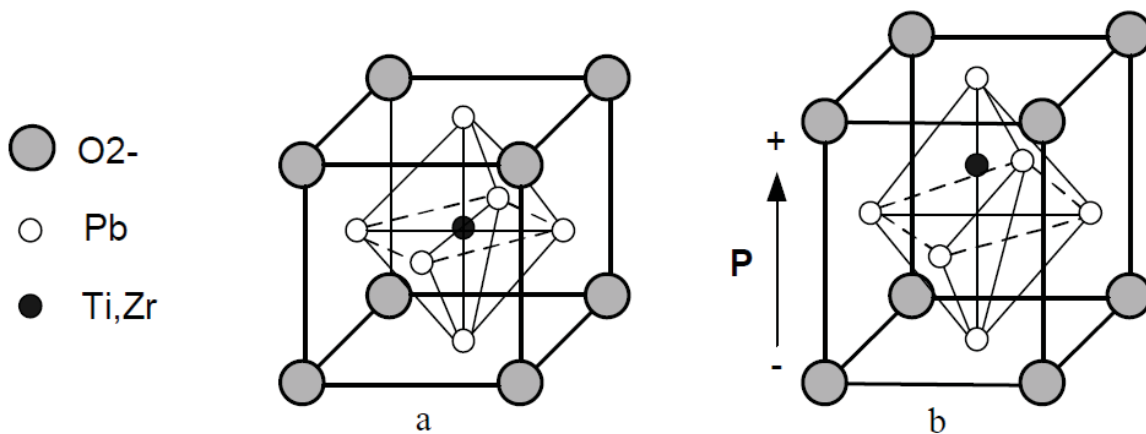


Figure 9: Perovskite structure

In the tetragonal state, each unit cell has an electric dipole, for example, there is a small charge differential between each end of the unit cell. A mechanical deformation (such as a compressive force) can decrease the separation between the cations and anions which produces an internal field or voltage. Also, if an electric field is applied along the

electric dipole, the tetragonal structure will deform due to the attraction or rejection forces between charges of the same or different polarities. The natural and synthetic crystals contain a monocrystalline structure which has the polarization orientated in the same direction as shown in Figure 10.

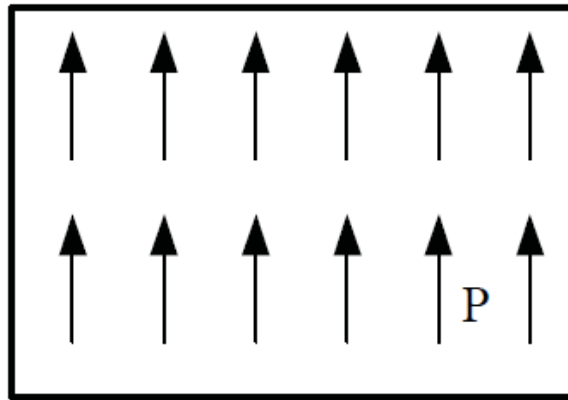


Figure 10: Polarization of crystals

In order to be of practical use, these crystals can only be cut in simple shapes, such as rectangular plates along the crystallographic axes. Moreover, certain synthetic piezoelectric materials called piezoceramic materials are used in order to obtain various geometries such as rings, tubes or disks. These materials are powders, which enable themselves to be sintered in any shape and be more useful for practical applications. In contrast with the crystals, some disadvantages exist that after they are sintered, the internal domains of polycrystalline structure have the polarizations randomly oriented as shown in Figure 11, and the global result of the piezoelectric effect is zero. To be able to use them as piezoelectric materials, one has to proceed to the re-orientation of the domains into one direction. This is usually done by a procedure called polling. During this procedure, the piezoelectric object is heated at a temperature above the Curie point

and a strong electric field E is applied in the direction one wants the piezoelectric effect to take place (shown in Figure 12). For the domains that have a polarization oriented in a different direction than the electric field, the interaction between the dipoles and the electric field generates a force on these electric dipoles and rotates them in the direction of the applied field. The temperature will be decreased gradually while the electric field is maintained. It will lead to the result of all sub-domains having the polarization oriented in the same direction after the temperature decreasing under the Curie point.

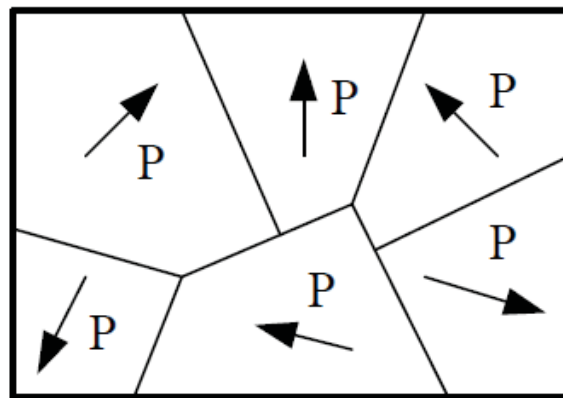


Figure 11: Polarization of the piezoelectric ceramic domains

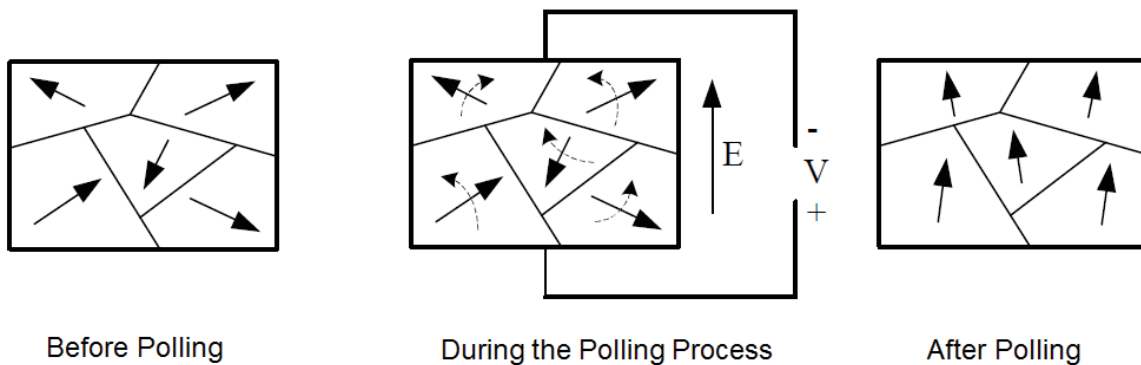


Figure 12: The polling process

2.4. Piezoelectric Actuator

For the initial investigations, a simple ceramic-disc “buzzer” transducer was obtained from Jaycar Electronics, as shown in Figure 13.

The known data for the buzzer is as follows:

- Diameter of nickel-alloy disk (D) 27.00mm
- Diameter of piezo-ceramic disk (d) 20.00mm
- Thickness of nickel-alloy disk (t) 0.10mm
- Total thickness (T) 0.34mm

The oscillation could be affected by the thickness of the nickel disk. The oscillation will be reduced if either the nickel is too thick or too stiff. Therefore, this piezoelectric buzzer (nickel-alloy disk thickness 0.10mm) was chosen for this study.

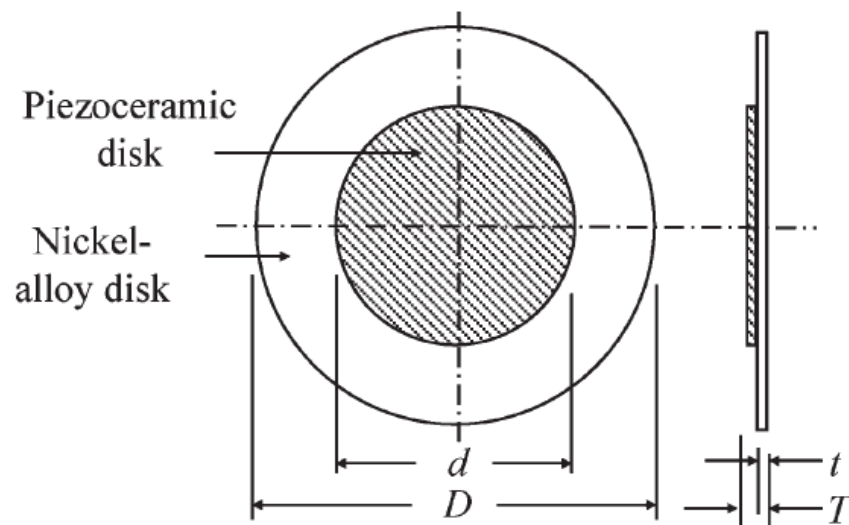


Figure 13: Schematic view of a piezoelectric buzzer

Chapter 3

System Configuration

3.1. Chapter Overview

A structure of the piezoelectric rotary motor with novel cyclic symmetric stator will be introduced and also the geometry parameter and material properties will be specified in this chapter. Furthermore, the novel cyclic symmetric stator structure carried with identical and evenly-spaced protrusion will be examined through finite element simulations. Particularly, the emphasis is placed on the behavior of the disk and fingers of the stator when different excitation frequencies and mode shapes are introduced into the structure. The fingers movement change in frequencies was observed while investigating the mode shapes.

3.2. Model Description

The objective of this thesis is to develop a novel cyclic symmetric stator which is driven by piezoelectric ceramic buzzers. Previous studies focus on combining two bending modes and a longitudinal mode of the actuators which employed dual-phase-driven ultrasonic actuators [13]-[16]. Those designs were still in large size and lack in output forces per volumes due to the driving principles, and the dual-phase-driven ultrasonic actuators. A dual-phase-driven ultrasonic actuator is believed to be a better fit for multi-degree-of-freedom mechanisms, however, it requires more time and cost to manufacture and is hard to miniaturize because their frequencies must correspond to each other. On the contrary, the single-phase-driven ultrasonic actuator can be made

with lower cost and is also easy to miniaturize. Hence, a novel cyclic symmetric stator design for applying the plural single-phase-driven actuators is developed for this thesis.

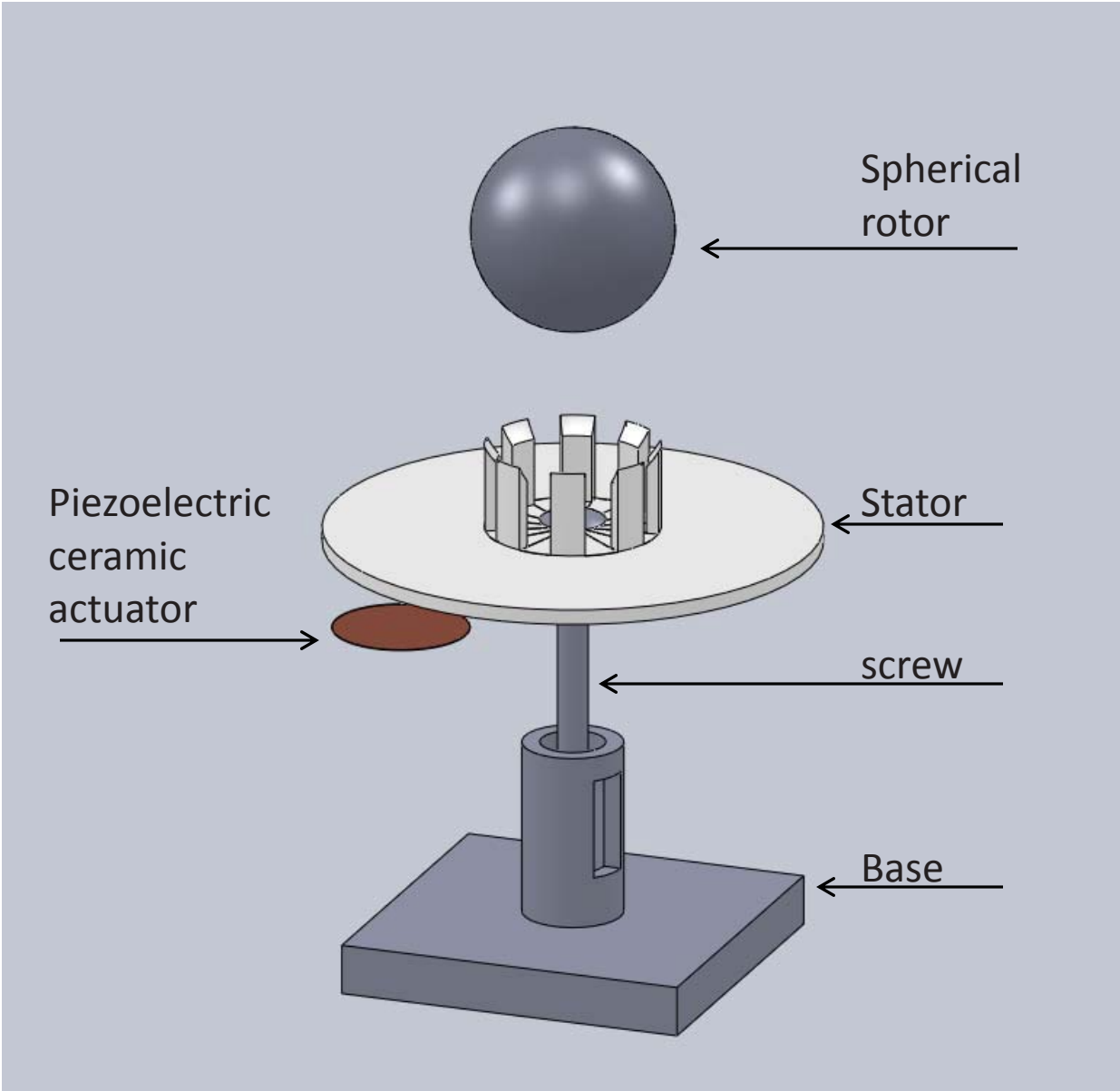


Figure 14: Structure of the piezoelectric rotary motor

In the beginning, the structure of proposed piezoelectric motor as illustrated in Figure 14 was built by using commercial finite element package (SolidWorks). As depicted in the plot, the model consists of four basic parts: the spherical rotor, the stator, the piezoelectric ceramic buzzer mounted on the stator and the base. Then, the design of mechanical components is required to be manufactured.

3.2.1. Rotor

The rotor is a hollow spherical-shape ball of size diameter 40mm. For the experimental observations, a ping-pong ball was used as an alternative for metal rotor due to technical difficulty of manufacturing a metal spherical-shape ball.

3.2.2. Stator

The proposed stator consists of disk and protrusion fingers, which was made of ABS material. The stator disk (Figure 15) with inside radius $\gamma_i=3.2\text{mm}$, outside radius $\gamma_o=49\text{mm}$ and the thickness of the disk $h=3\text{mm}$ was physically clamped around γ_i with base by a bolt screw. There are eight evenly-spaced protrusion fingers on the surface of the stator disk. The arch-shape tip was designed on each of the protrusion fingers, which holds and drives the spherical-rotor. The rotor in contact with the surface point of the fingertips was driven by frictional force. For the purpose of saving manufacturing time and reducing cost of the material, the rapid prototype technology was employed to manufacture the cyclic symmetric stator.

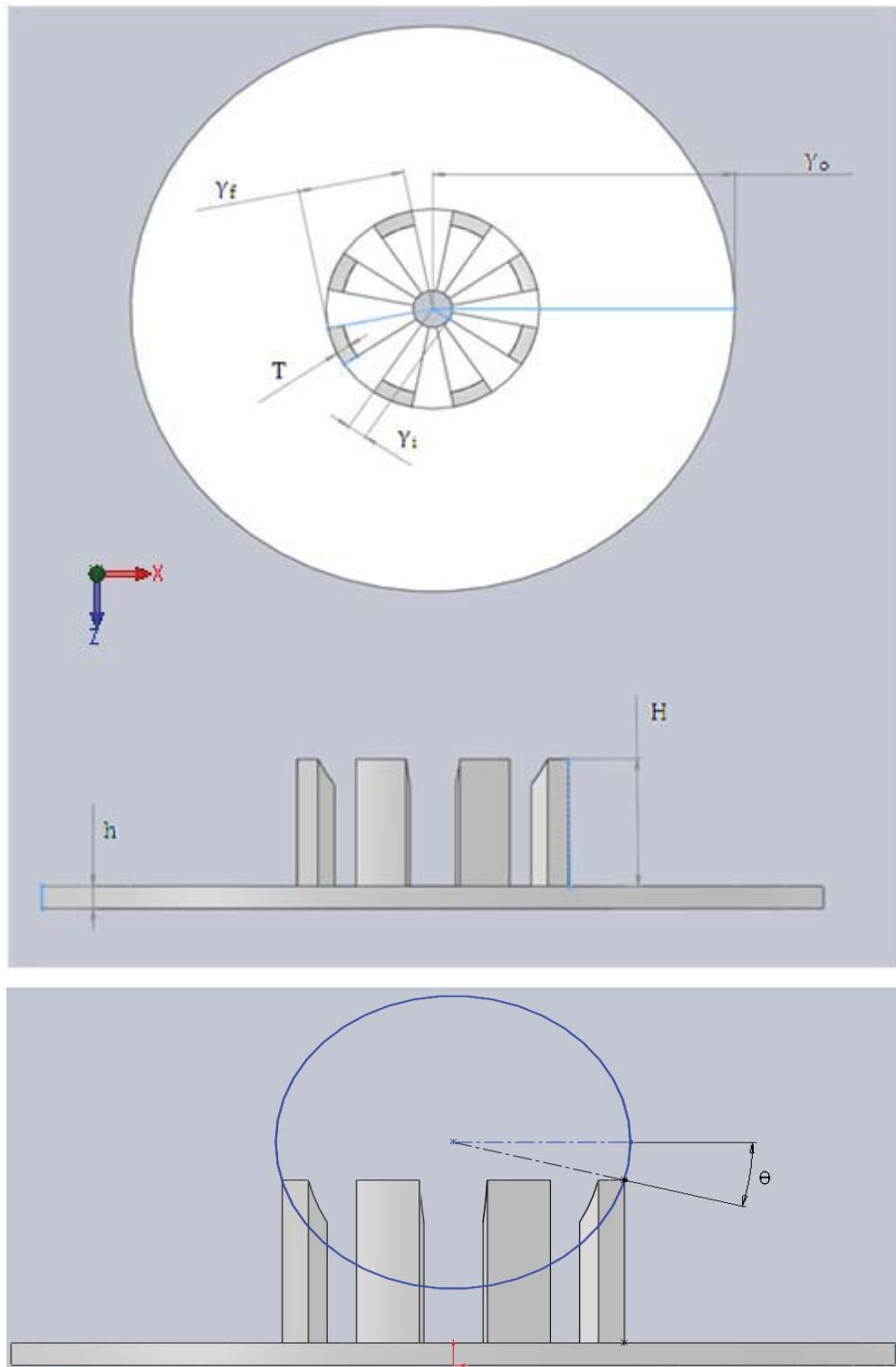


Figure 15: schematic of the cyclic symmetric stator

3.2.3. Piezoelectric ceramic buzzer

The piezoelectric ceramic buzzer consist of nickel-alloy disk with diameter 27mm and piezo-ceramic disk with diameter 20mm, which was attached to the surface underneath the cyclic symmetric stator. In order to gain optimal actuation result, it is essential to have strong bonding between the stator and the piezoelectric ceramic. Thus, in order to achieve this, epoxy adhesive was applied at each interface. This piezoelectric ceramic buzzer was driven by the sinusoidal wave which is generated by the function generator and is enhanced by the power amplifier circuit.

3.2.4. Base

The base is a moveable substrate with size of $70 * 70 * 45 \text{ mm}^3$, which is used to clamp the cyclic symmetric stator.

3.3. Finite Element Analysis

A finite element analysis is very important for designing a novel piezoelectric rotary motor with cyclic symmetric stator because it offers information about possible driving frequency and rotational direction of the motor. In order to examine the displacement and structure response on the stator disk and protrusion fingers:

- Proposed cyclic symmetric stator solid model was created
- Material properties were specified

Property	Value	Units
Elastic Modulus	2000000000	N/m ²
Poissons Ratio	0.394	N/A
Shear Modulus	318900000	N/m ²
Density	1020	kg/m ³
Tensile Strength	30000000	N/m ²
Compressive Strength in X		N/m ²
Yield Strength		N/m ²
Thermal Expansion Coefficient in X		/K
Thermal Conductivity	0.2256	W/(m·K)
Specific Heat	1386	J/(kg·K)
Material Damping Ratio		N/A

- The boundary condition of the cyclic symmetric stator was defined
- Mesh was generated (Figure 16) and then the solution for modal analysis, mode shape and natural frequencies were obtained.

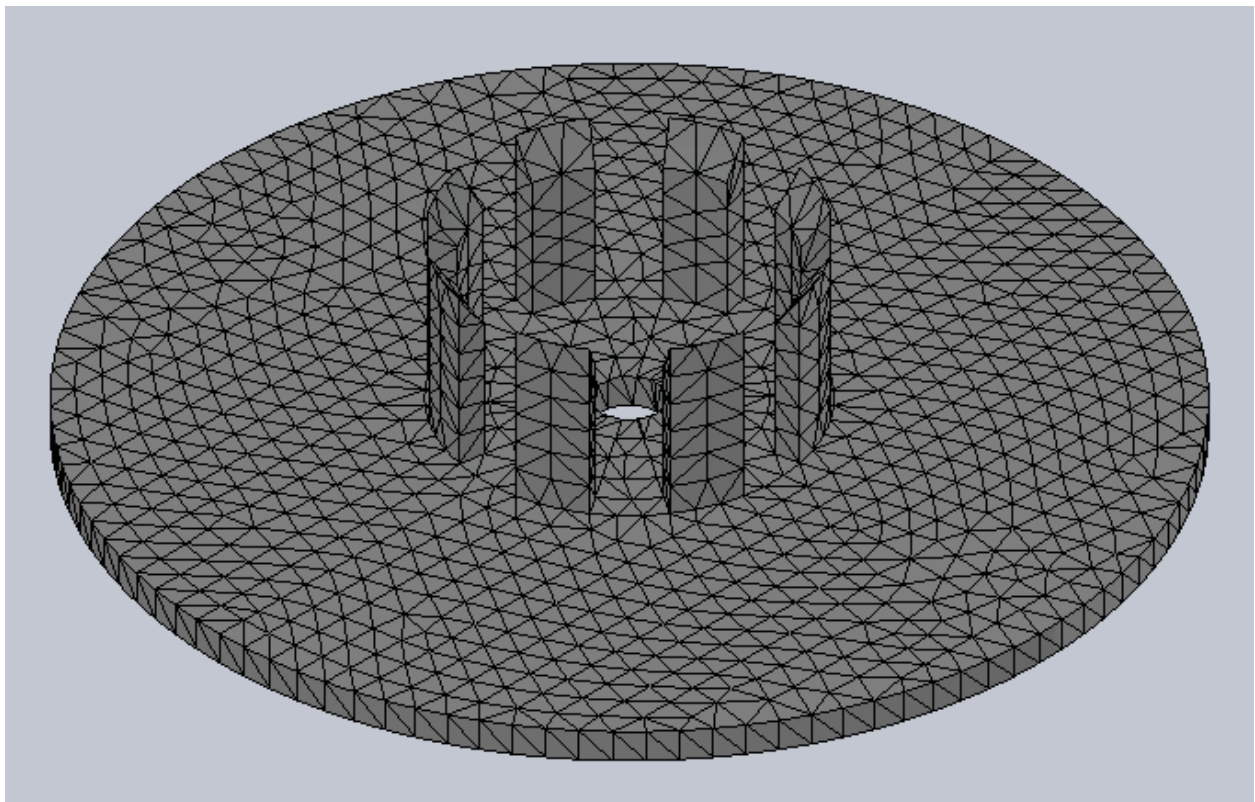


Figure 16: Mesh of the cyclic symmetric stator model with boundary condition

Following the nomenclature and mode structure characterized in reference [17]-[18], letter P is given to distinguish the cyclic symmetric stator's vibration modes from those modes denoted as (m, n) in axis-symmetric case, where m represents number of nodal circles and n is the number nodal diameters, respectively. For instance, $P(0, 1)$ stands for the cyclic symmetric stator's vibration mode having zero nodal circle and one nodal diameter in axis-symmetric disk case.

Natural frequencies and mode shapes of the cyclic symmetric stator model are plotted in Figure 17. It is observed that the mode shapes in the first two mode ($P(0, 1)$) repeats itself. The natural frequencies of both modes are almost the same, which are at 252.98Hz and 253.21Hz respectively. The 90° shifting structure responses can be seen on the morphing display which represent sine and cosine oriented components. The deformation of stator's protrusion fingers was sectioned by the nodal line into two parts and both deformations occurred at the same direction.

Followed by the fourth and fifth mode shape $P(0, 2)$, both of the mode shapes have the same characteristics as $P(0, 1)$; which shows the same deformation in the mode shape and very similar frequency value on both modes. Both of the deformation movement on the protrusion fingers are the same, where the distorted behavior is symmetrical but on the opposite direction.

The seventh and eighth mode shape in Figure 18 has similarly depicted two repeated mode shapes ($P(0, 3)$). The features of disk deformation and natural frequency were same as discussed in the aforementioned two sets of mode shapes ($P(0, 1)$ and $P(0, 2)$). However, in $P(0, 3)$ the behavior of the protrusion fingers is apparently affected by the stator disk's deformation, especially when the protrusion finger is located within or without the nodal diameter. Additionally, when the protrusion fingers are located within the nodal diameter, the fingers deform towards the left. Moreover, the deformation moves forward and backward while the fingers are located without the nodal diameter.

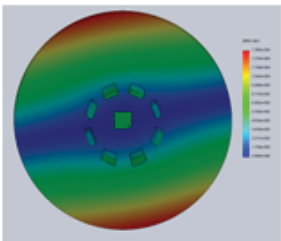
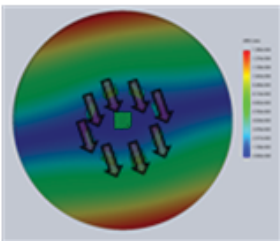
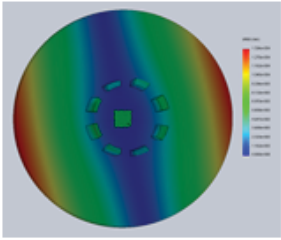
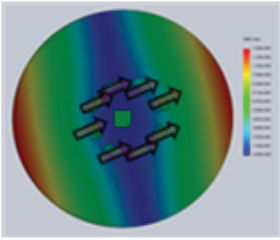
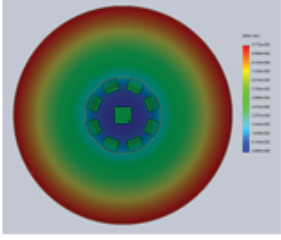
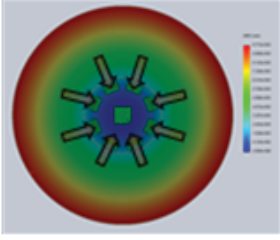
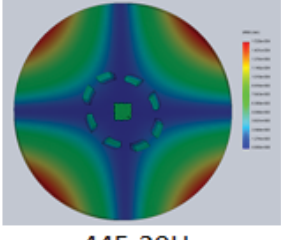
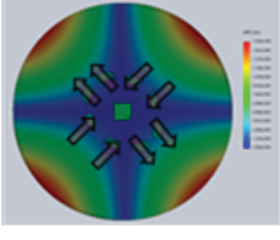
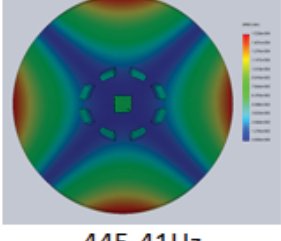
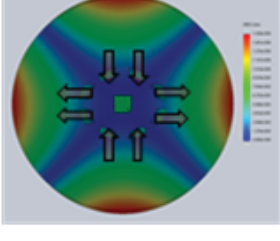
	Mode Shape	Protrusion Finger Deformed Direction
1	 <p>252.98Hz</p>	
2	 <p>253.21Hz</p>	
3	 <p>345.2Hz</p>	
4	 <p>445.29Hz</p>	
5	 <p>445.41Hz</p>	

Figure 17: Simulation result from Solidworks (Mode Shape 1~5)

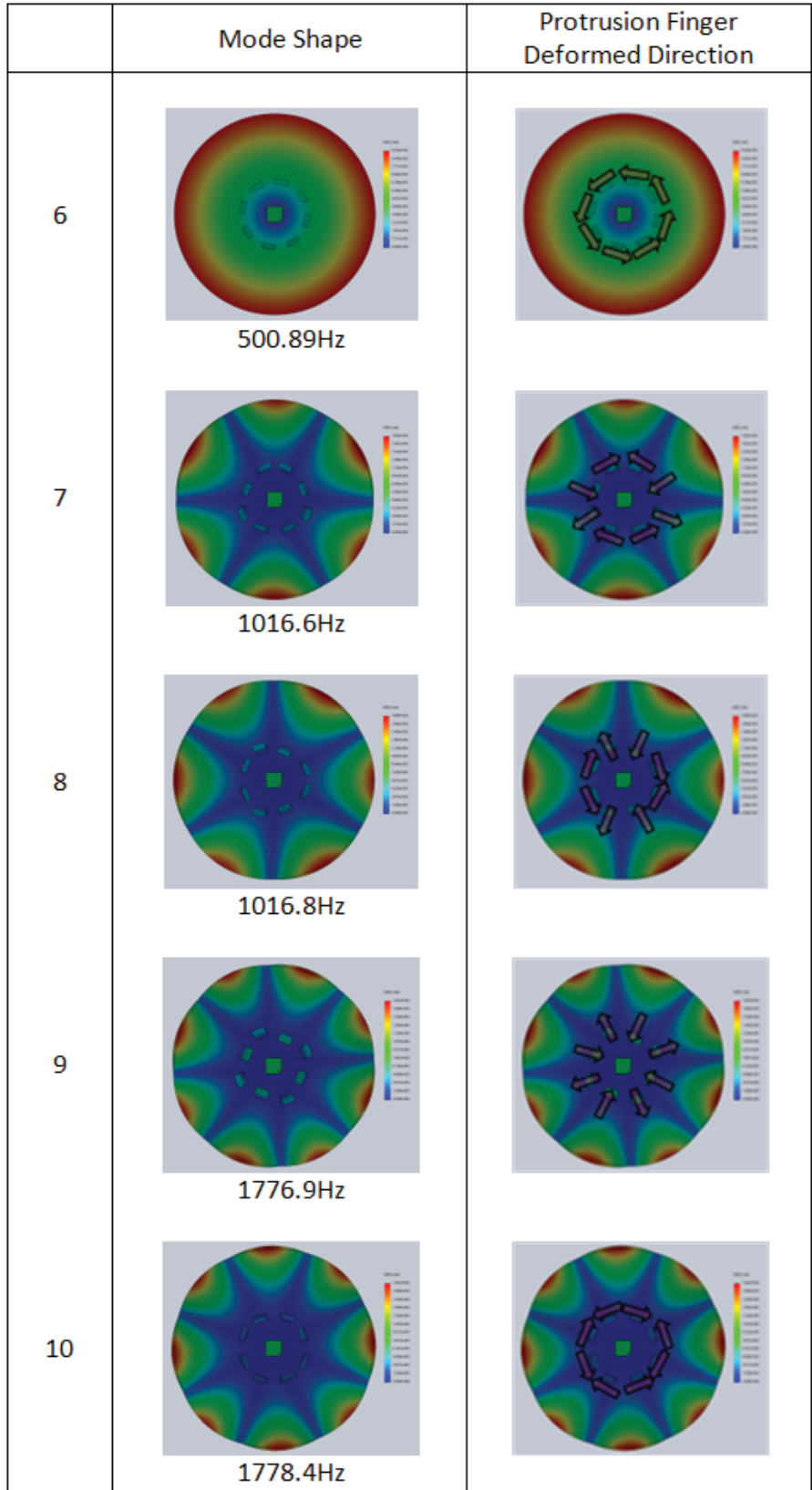


Figure 18: Simulation result from Solidworks (Mode Shape 6~10)

As mentioned in the previous paragraph, the deformation on the stator disk and fingers repeats itself in the same modes (sine and cosine oriented) with slightly different frequency (around 1Hz). There is an interesting finding in the following two sets of mode shape $P(0, 4)$ shown in Figure 18. The mode shape shows the same structural response on the stator disk in $P(0, 4)$, but the response tends to split at the fingers. This proposed cyclic symmetric stator design has eight evenly-spaced protrusion fingers. All of the protrusion fingers were arrayed without the nodal diameters when excited at 1776.9Hz as shown in mode shape 9. The nodal diameter shifts to a certain degree when the frequency is slightly changed to 1778.4Hz. At the same time, the locations of the protrusion fingers were also changed within the nodal diameters due to the frequency change. In general, there will not be any deformation on the protrusion finger when the fingers are arrayed on the nodal diameter. Due to the characteristics mentioned above, the movement of the deformed protrusion fingers was completely different from the previous pattern $P(0, 1)$ to $P(0, 3)$. The protrusion finger deformation is no longer repeated although it still repeats on the stator disk. Based on the observation, an assumption can be made that the location between the protrusion fingers and nodal diameters can affect the mode shape change especially in the protrusion fingers' deformed behavior.

In order to verify the phenomenon shown in $P(0, 4)$ which is related to the cyclic symmetric stator design, the protrusion fingers on the stator has been modified as shown in Figure 19. The number of protrusion finger has been changed to four and six in $P(0, 2)$ and $P(0, 3)$. In the earlier section, the mode shapes was repeated in both $P(0, 2)$ and $P(0, 3)$ modes. However, the mode shapes split when the number of the protrusion fingers changed in both modes.

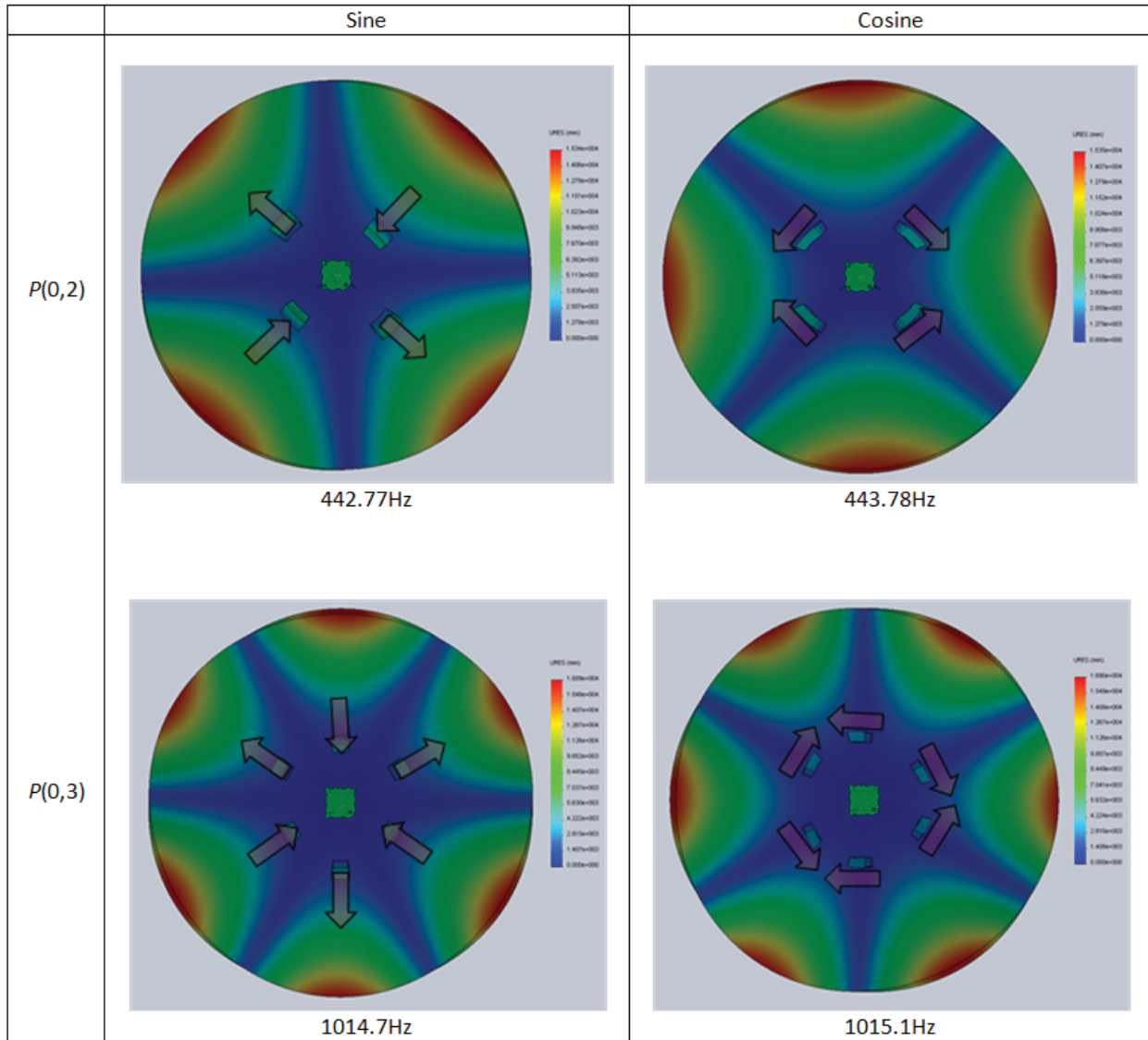


Figure 19: Modified cyclic symmetric stator with 4 and 6 evenly-spaced protrusion fingers in $P(0,2)$ and $P(0,3)$ respectively

In this FEM simulation, it was observed that the proposed stator is an axis-symmetric disk structure. The vibration modes of the stator are classified as being either doublet (in which case two linearly independent sine and cosine-oriented vibration modes of common frequency exist) or as singlet (where the frequency is an isolated root of a characteristic equation, and the vibration mode itself is axis-symmetrical). Those two classes of modes are further categorized according to the numbers m and n of nodal circles and diameters respectively [17]. It is found that the deformation relations between stator protrusion fingers and nodal diameters are significantly associated. Although the distortion of the stator disk behaves the same, different number of protrusion finger design can alter the fingers' movement directions under certain excitation.

3.4. Chapter summary

This chapter has presented a novel design of the piezoelectric rotary motor with cyclic symmetric stator. The schematic of the piezoelectric rotary motor was discussed and each part of the motor was introduced. The natural frequencies and structure responses of the cyclic symmetric stator were examined by using finite element approach. The focus was placed on the structure response between stator disk and protrusion fingers. Moreover, the movement of the stator disk and protrusion finger in different mode shapes has been observed. Based on the observation results, the mode shape of cyclic symmetric stator split and repeated in different frequencies. With the proposed cyclic symmetric stator design, the mode shape repeated in $P(0, 1)$, $P(0, 2)$ and $P(0, 3)$ but split in $P(0, 4)$.

In this mode shape ($P(0, 4)$), the mode shape displayed the same distortion on the stator disk in both sine and cosine oriented components. However, completely different distorted directions were found on the protrusion fingers. This interesting phenomenon can also be duplicated in those repeated modes ($P(0, 2)$ and $P(0, 3)$) when the number of protrusion fingers is changed to match the nodal diameters. According to the

modification on stator design, the number of the protrusion fingers exposed significant association with the nodal diameters. As a result, this feature can be employed to determine driving direction in the future experiment.

Chapter 4

Parametric study of the cyclic symmetric stator

4.1. Chapter Overview

The structure response of the cyclic symmetric stator disk and protrusion fingers was investigated in the previous chapter. The split mode patterns have been found on the protrusion finger in $P(0,4)$. Due to the novel phenomenon found in Chapter 3, the deformation movement performance of the protrusion fingertips in both split structure responses in $P(0,4)$ will be further investigated by parametric studies in this chapter. The parametric studies of displacement strength variation and in-plane bending deformation angle of the protrusion fingertips will be examined. The data that obtained from finite element simulation result will be used to evaluate through Fourier coefficients of sine and cosine oriented components.

4.2. Parametric study

According to the simulation results made in the previous chapter, the displacement strength at outer disk edge indicated higher value than at inner edge as shown in Figure 17 and Figure 18. However, it is hard to find the deformation perform on the protrusion fingers from those figures. In order to obtain optimal performance of the protrusion finger movement of the stator, the different contact angle between stator and rotor will be used as variables in the parametric studies. The two parameters, displacement strength and in-plane bending angle of the fingers, will be examined in this section.

The contact angle varied from 0°, 15°, 30°, 45° and 60°, respectively. The protrusion fingertips height was at fixed value of 20mm. The ratio between finger radius and disk radius and the contact area between rotor and fingertips was shown in Table 1.

θ	Finger radius (r_f)	Disk radius (R)	r_f/R	Contact area	H
0°	20	49	40.82%	608.37	20
15°	19.32	49	39.43%	354.79	20
30°	17.32	49	35.35%	215.48	20
45°	14.14	49	28.86%	133.21	20
60°	10	49	20.41%	76.65	20

Table 1: Detail setting data of different contact angle

4.2.1. Displacement variation with varying contact angle

The structure responses of the cyclic symmetric stator in five different contact angles were simulated as illustrated in Figure 20 to Figure 23 for the nominally four nodal diameters mode. The probed data of the protrusion fingertips from the simulation was employed to evaluate displacement strength through MATLAB analysis. The displacement strength of the protrusion fingertips can be written in classical Fourier expansion of

$$u(\vartheta) = \sum_{k=0}^{\infty} A_k \cos(k\vartheta) + B_k \sin(k\vartheta) \quad (4.1)$$

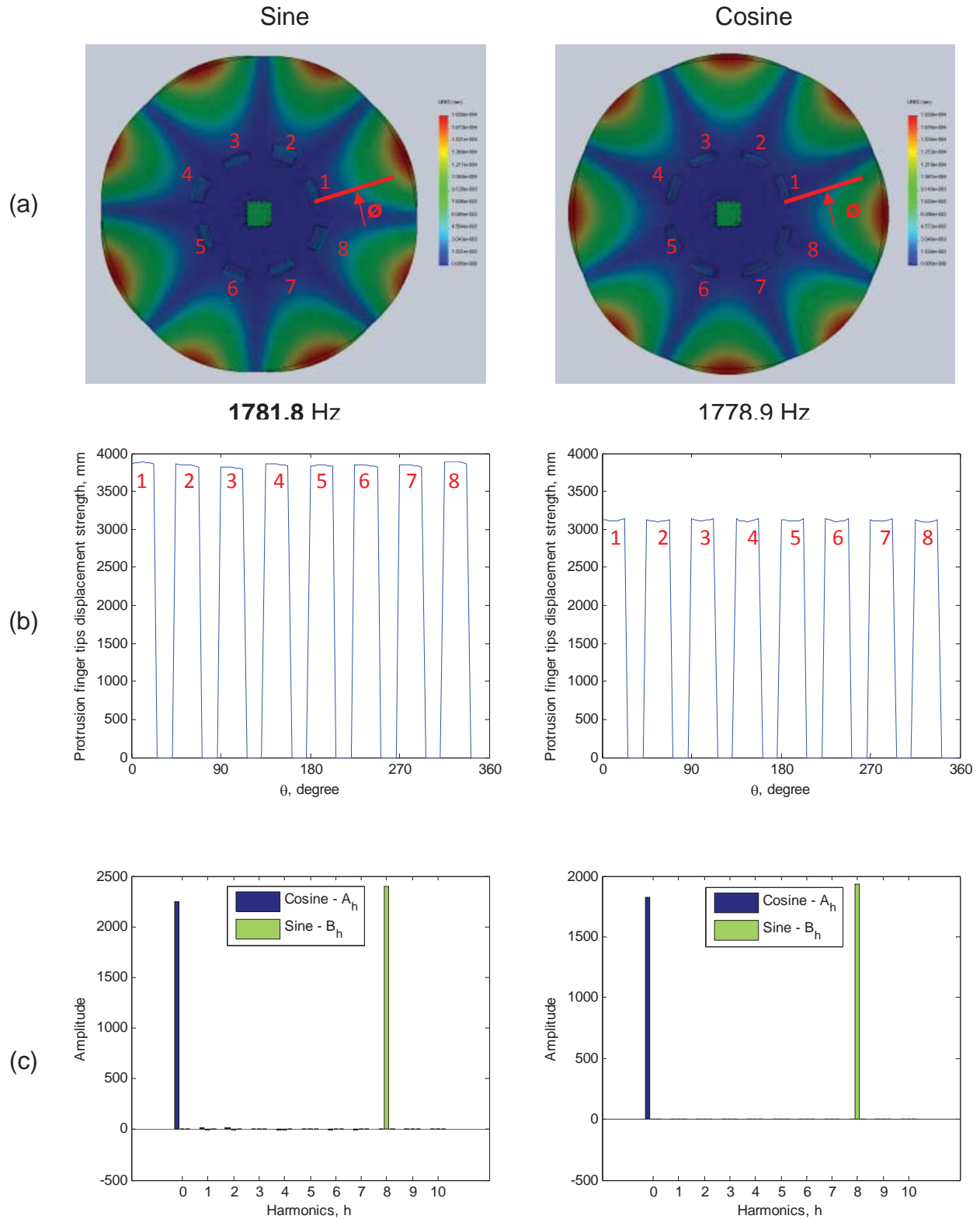


Figure 20: Contact angle at 0° - (a) nodal patterns and (b) the displacement strength of protrusion fingertips. (c) the corresponding Fourier coefficients

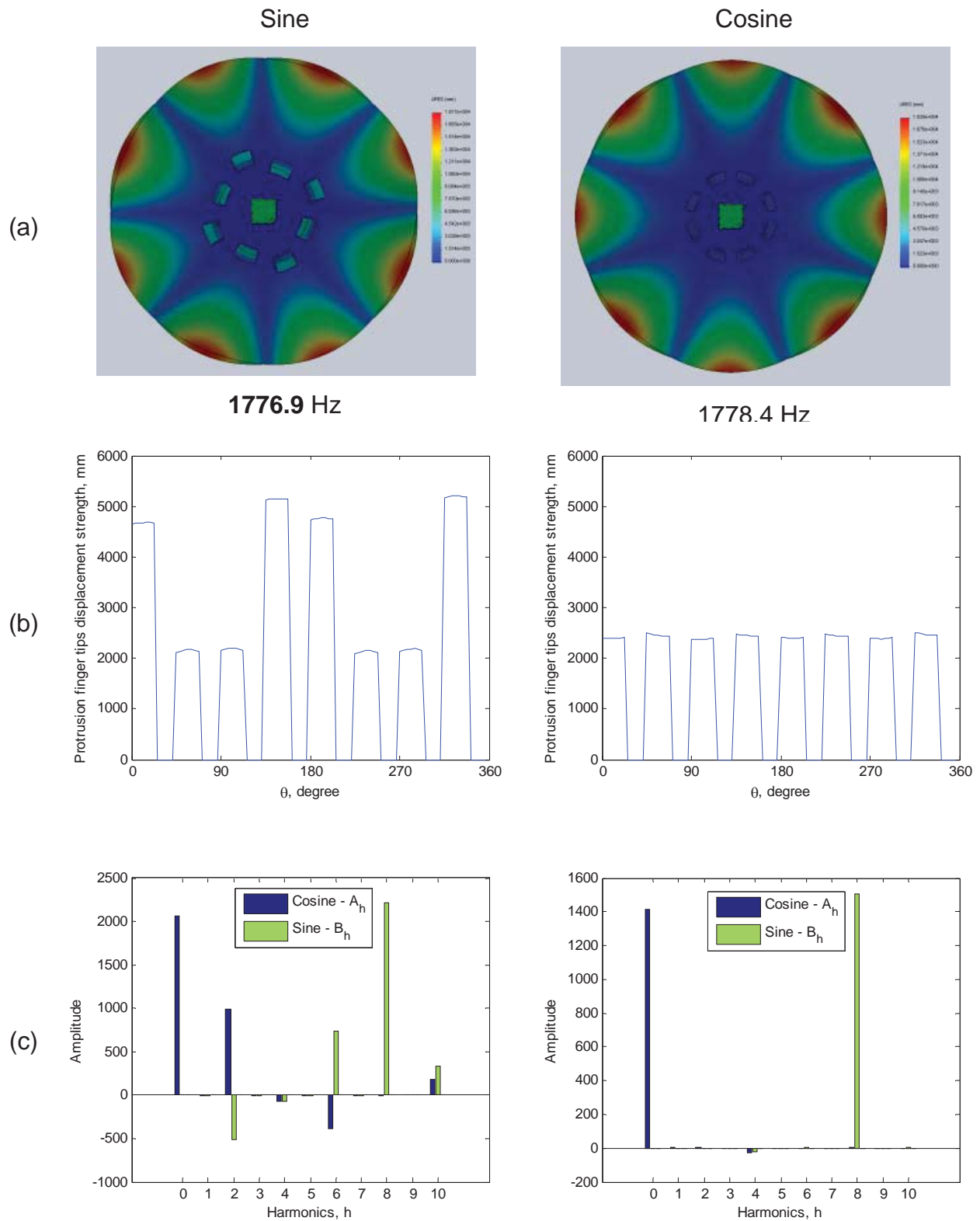


Figure 21: Contact angle at 30° - (a) nodal patterns and (b) the displacement strength of protrusion fingertips. (c) the corresponding Fourier coefficients

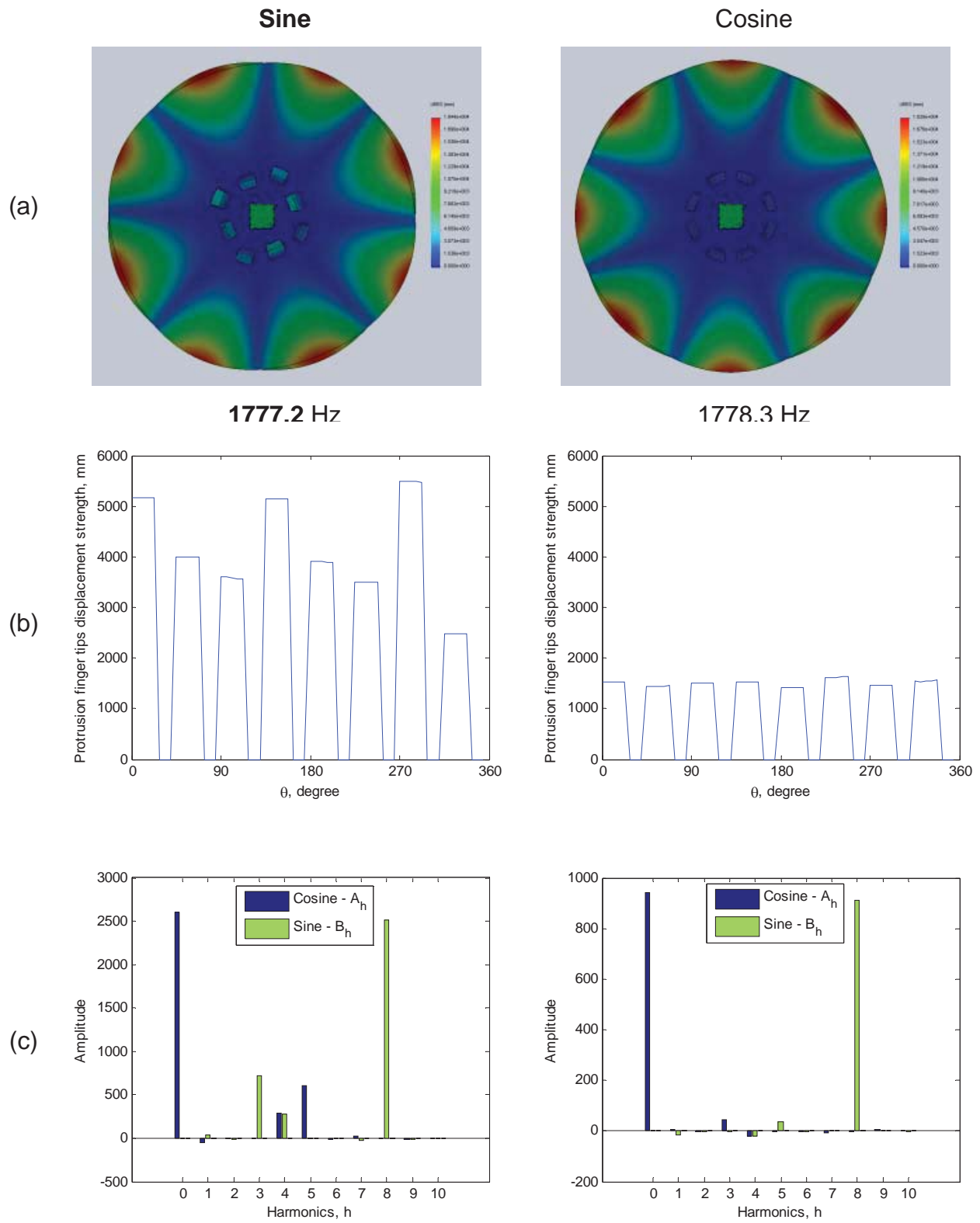


Figure 22: Contact angle at 45° - (a) nodal patterns and (b) the displacement strength of protrusion fingertips. (c) the corresponding Fourier coefficients

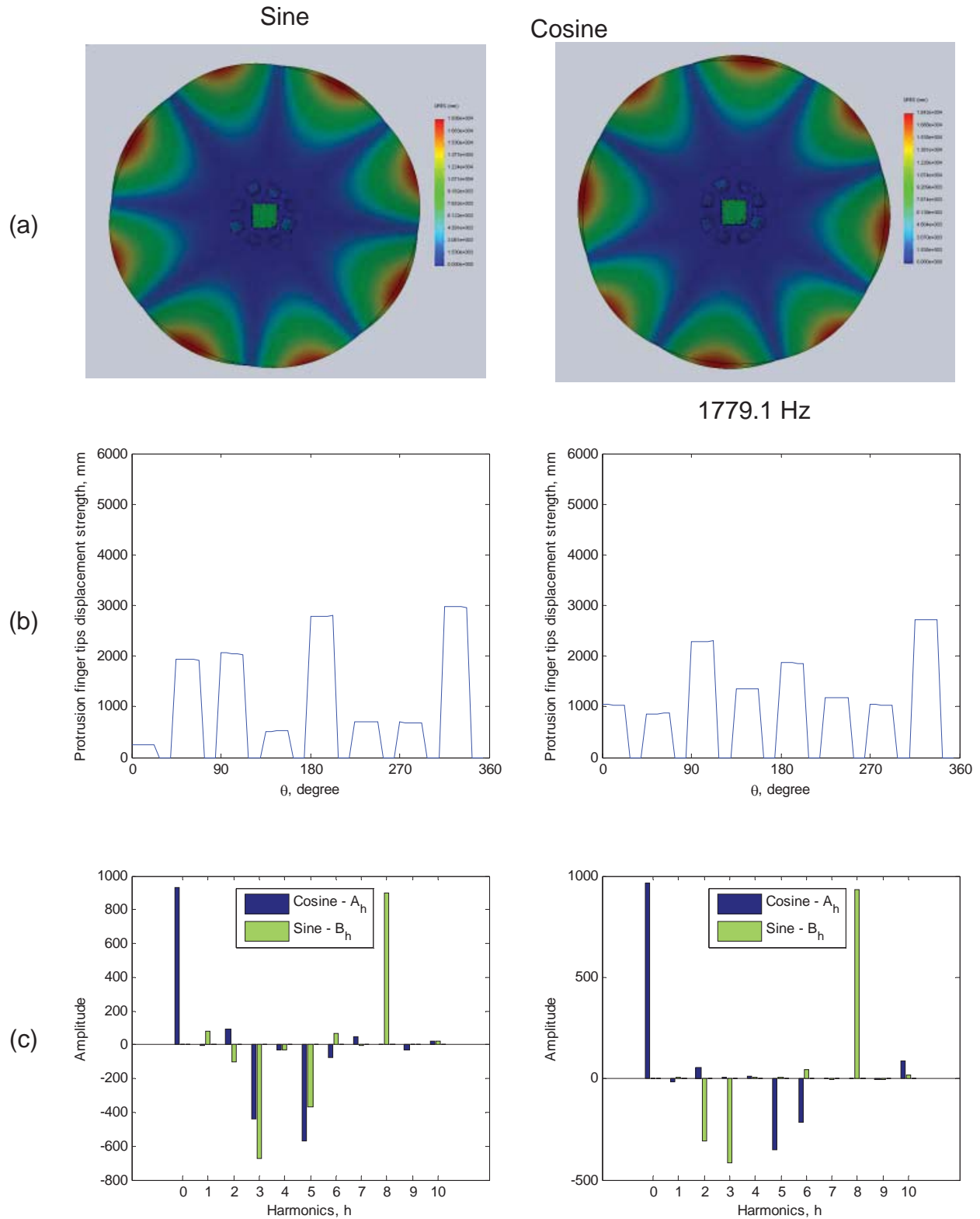


Figure 23: Contact angle at 60° - (a) nodal patterns and (b) the displacement strength of protrusion fingertips. (c) the corresponding Fourier coefficients

In order to represent the distorted appearance for the mode around the protrusion fingertips where \varnothing is the circumferential measure starting from first protrusion fingertip. The nodal patterns, displacement strength and Fourier amplitude of the structure response of the split modes at contact angle 0° depicted in Figure 20. The Fourier amplitude was plotted up to $k=10$ harmonic count in Figure 20(c). The eight peak displacement strength value represented each of the fingertips (starting from \varnothing shown in Figure 20(a)). The displacement strengths in Figure 20(b) were around 3800mm and 3150mm in sine and cosine oriented components respectively. Each of the fingertips revealed almost the same displacement strength in both sine and cosine modes. However, it was noted that a slight difference in displacement strength was displayed on each of the fingertips. These interesting characteristic can be further investigated in the future study. In comparison with contact angle 0° , a higher displacement strength value was shown at contact angle 15° , however other features were almost the same as at 0° . In the earlier section, the higher displacement strength was found at the disk's outer edge compared to its inner edge. Contrastingly, higher displacement strength on protrusion fingertips was revealed at contact angle 15° (approximately 5000mm) compared to 0° (approximately 4000mm).

At contact angle 30° , the displacement strength of each protrusion fingertips significantly changed (shown in Figure 21). The displacement strength of each fingers were no longer of the same value; the highest strength value was revealed by the 4th and 8th finger ($\pm 5000\text{mm}$), followed by 1st and 5th finger ($\pm 4700\text{mm}$). The rest of the fingers' strength were only at 2000mm. Based on this observation, it is noted that these four fingers (1st, 4th, 5th and 8th) located symmetrically dominated the main role of rotor driving. As a result, the rotor movement was moving in a diagonal direction.

Similarly, at contact angle 45° (Figure 22) a significant difference was also exhibited on protrusion fingertips and the displacement strength appeared the same trend as those fingers at 30° contact angle; dominant fingertips appeared selectively. However, the dominant fingertips in 45° differ from that of 30° ; dominant fingertips were not as prevailing and not located symmetrically, resulting in an erratic vertical motion. In the

last contact angle (60°), it is observed that the structure response is totally different from the previous angles as the finger radius is too narrow (10mm) to match the nodal diameters (Figure 23). Additionally, nodal pattern no longer repeated. It is noted that these split mode response will no longer be duplicated when the finger radius is too narrow (10mm). Hence, simulation beyond 45° is out of question to achieve optimal displacement in split modes.

4.2.2. In-plane deformation angle with varying contact angle

In the last section, displacement strength variation of each protrusion finger was found at different contact angle. It can also effect on the direction of the rotor. In this section, the in-plane bending deformation angle of each fingertip will be investigated. The bending deformation angle (Φ) with respect to x and z direction of the fingertips displacement as

$$\Phi = \tan^{-1} \frac{x}{z} \quad (4.2)$$

was calculated to evaluate the fingertip movement change. Figure 24 illustrates a 90-degree phase difference between sine and cosine mode same as that shown in nodal pattern of contact angle 0°. The bending deformation angle decline on each fingertip in cosine oriented component; bending motion angle still remains the same in sine mode. It is noted that the decline angle can affect the twisting result of the rotor. At contact angle 15°, the same bending deformation pattern arose as at 0°. Hence, based on the observed result, the rotational variation is more likely to alter by introducing the cosine oriented component in these two angles.

The significant change was found between sine and cosine modes at contact angle 30° shown in Figure 25; the bending deformation pattern was no longer at 90-degree shift from sine to cosine mode. On the one hand, the bending deformation angle in sine mode depicted a sunken bow shape at the fingertips, which means the fingertips

distorted at the center rather than a decline deformation at one side in cosine mode. The sunken bow shape fingertips results in a movement at a fixed angle, rather than moving at a diagonal angle with the decline deformation's angle. On the other hand, the high bending deformation angle ($\pm 80^\circ$) revealed in four fingertips (1st, 4th, 5th and 8th). As finger 1 and 8 is at a negative bending deformation angle, while finger 4 and 5 is at a positive angle, this result in a clockwise rotational motion.

At contact angle 45° , the bending deformation pattern switched back to the same as 0° and 15° . It also indicated the decline bending deformation angle on the protrusion fingertips in cosine mode. Moreover, the bending deformation angle revealed inconsistency in both sine and cosine mode at contact angle 60° as shown in Figure 26. Due to the finger radius is too narrow, the bending angle affected each other. It is hard to find any patterns and relations in both sine and cosine mode.

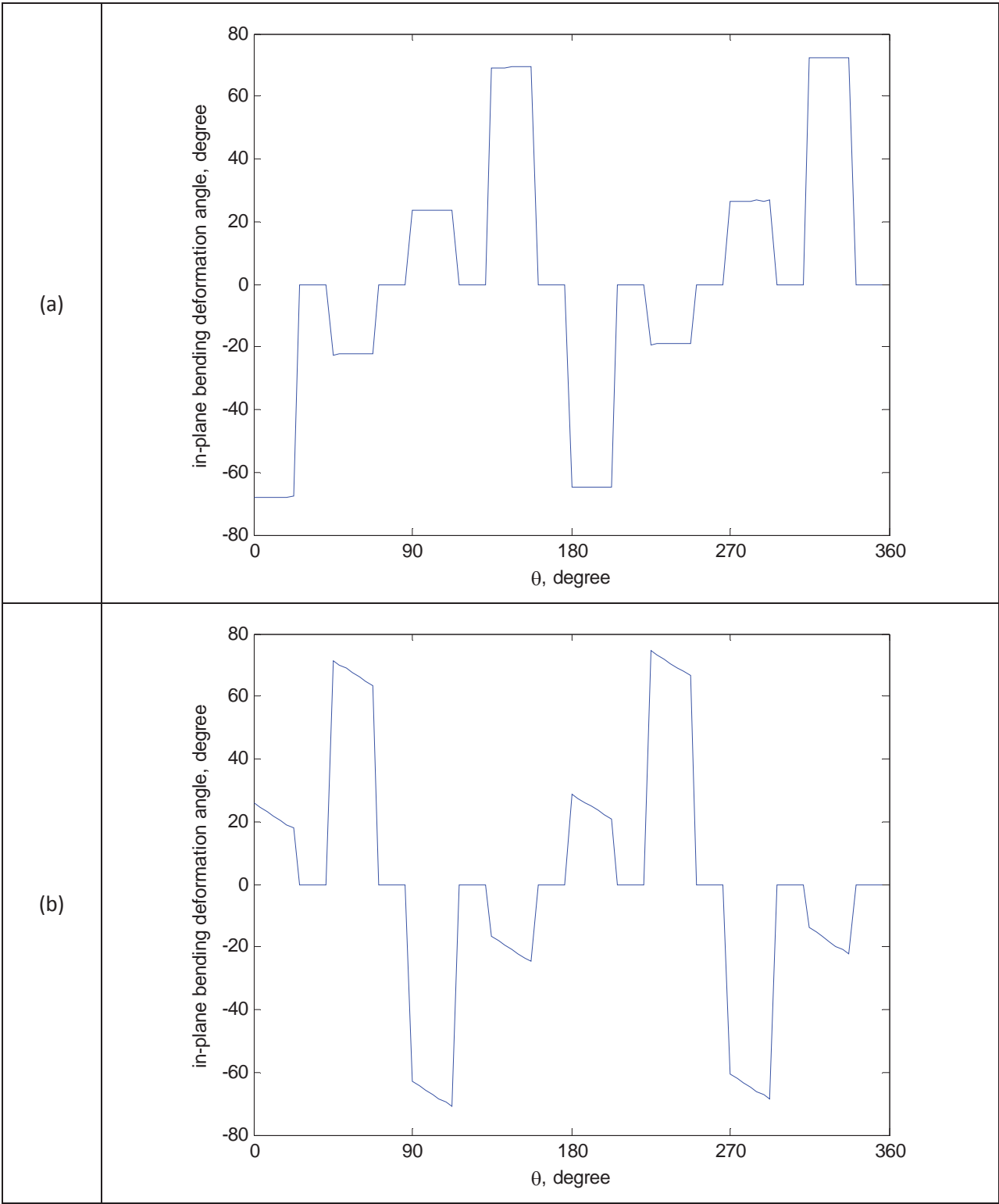


Figure 24: Contact angle at 0° - Protrusion fingertips deformed angle in (a) sine and (b) cosine oriented components

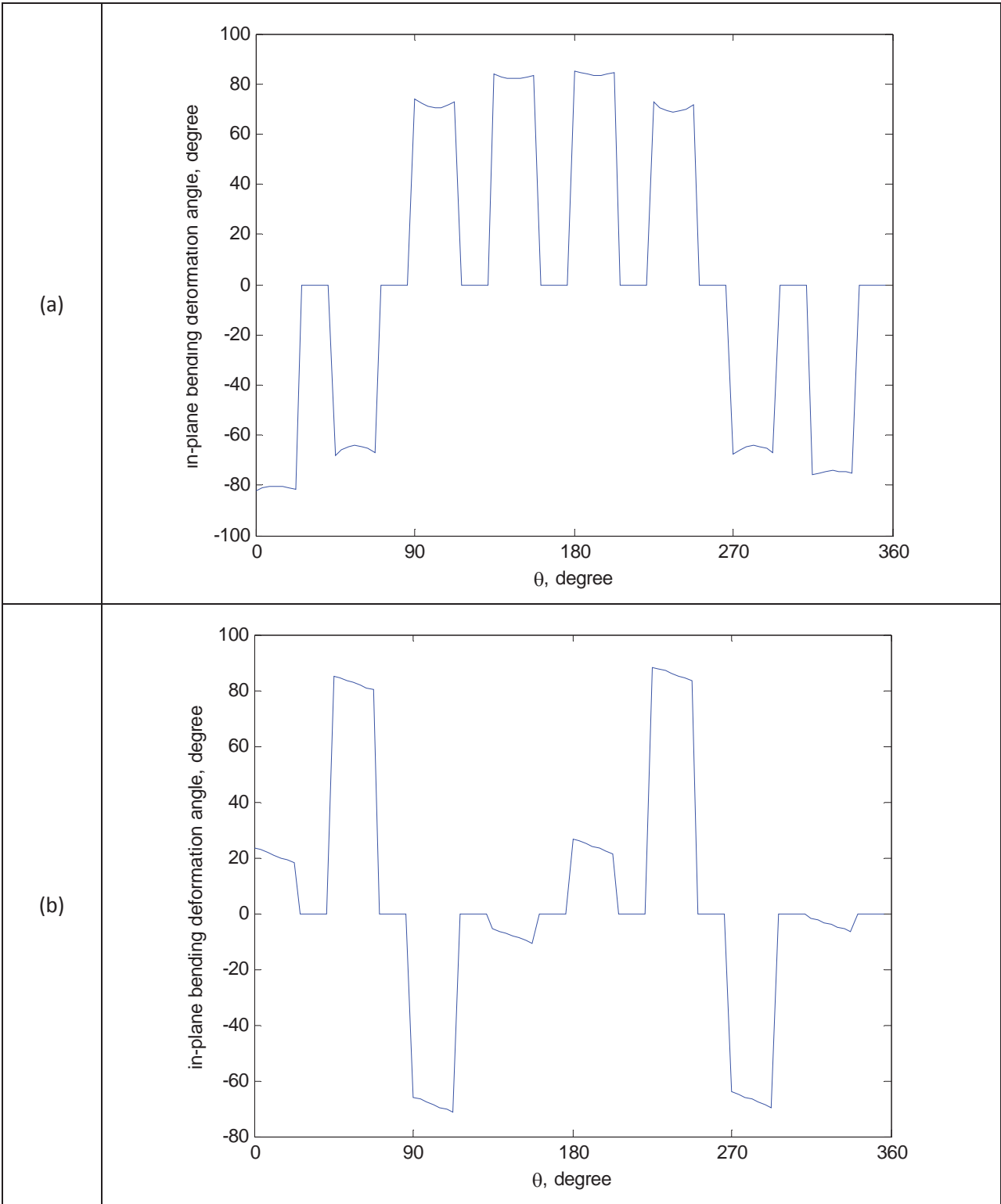


Figure 25: Contact angle at 30° - Protrusion fingertips deformed angle in (a) sine and (b) cosine oriented components

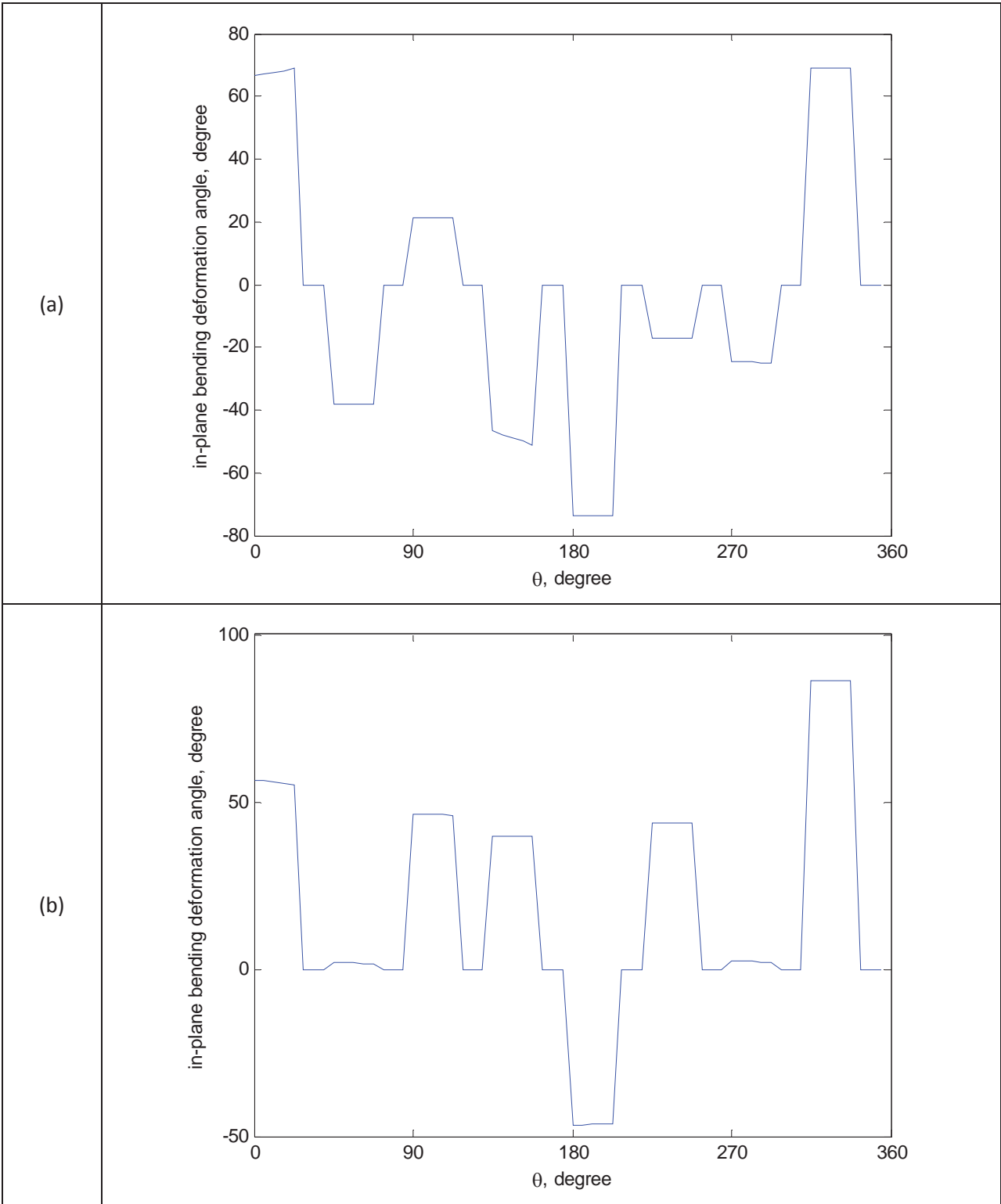


Figure 26: Contact angle at 60° - Protrusion fingertips deformed angle in (a) sine and (b) cosine oriented components

4.3. Chapter summary

Parametric studies for displacement variation and in-plane bending deformation with varying contact angle between stator and rotor have been conducted for identification of movement performance of the protrusion fingertips. The variation of displacement strength value was found in each protrusion fingertips in different contact angle. Certain fingertips were found having high displacement strength value and dominated the bending motion in both contact angle at 30° and 45°. Especially, at contact angle 30°, four fingers (1st, 4th, 5th and 8th) located symmetrically dominated the main role of rotor driving in a diagonal direction. The same bending deformation angle patterns were discovered in both sine and cosine modes at contact angle 0°, 15° and 45°. On the contrary, a high bending deformation angle ($\pm 80^\circ$) revealed in four fingertips (1st, 4th, 5th and 8th) at 30° contact angle, this result in a clockwise rotational motion. The nodal pattern was no longer repeated at contact angle 60°, meanwhile, the displacement strength value revealed much smaller than the other contact angles. In addition, It is hard to find any patterns and relations in both sine and cosine mode due to the bending angle was affected by each fingers.

Chapter 5

Experimental Result

For experimental testing, the proposed piezoelectric rotary motor with cyclic symmetric stator will be presented in this chapter. The detail experimental setup will be discussed in the following section. The piezoelectric buzzer is attached to the cyclic symmetric stator prototype for driving the stator's natural frequencies and also the piezoelectric buzzer mounting location will be reviewed by using the Chlandi figures. This experimental prototype is built to examine the consistency with the aforementioned simulation result.

5.1. Experimental setup

For rotation experimental testing, the diagram of the experimental platform is show in Figure 27 and is comprised of the following components:

- the piezoelectric rotary motor model
- the function generator – use to provide a voltage with variable frequency, which is used to drive the power amplifier circuit
- the power amplifier circuit - amplify the voltage received from the function generator and the amplified voltage is applied to the piezoelectric ceramic buzzers
- the oscilloscope - use to monitor the voltage supplied to the piezoelectric ceramic buzzers

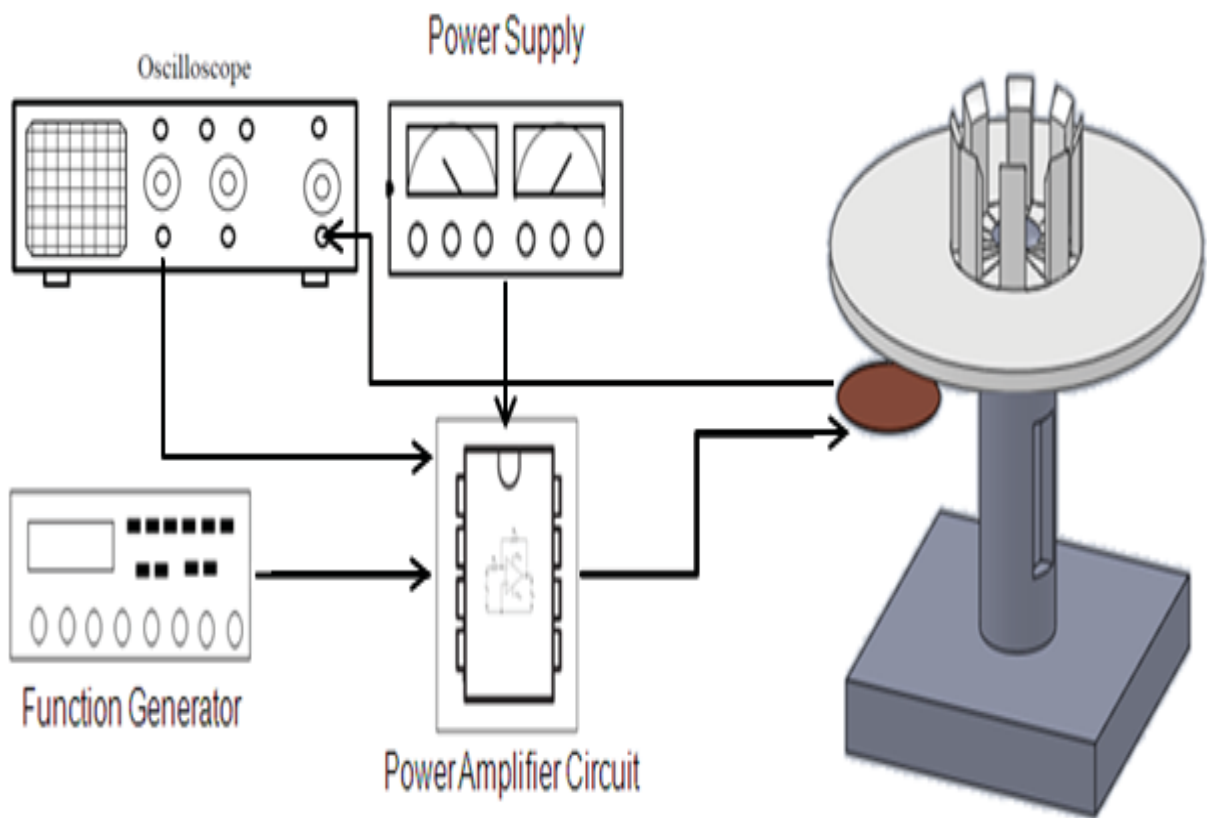


Figure 27: Piezoelectric rotary motor experimental setup

5.2. Experimental result

In Chapter 3 of this thesis, the cyclic symmetric stator was modeled using commercial finite element package. By using this software, the natural frequencies and mode shapes have been simulated. In order to validate the optimal movement performance of protrusion finger in terms of the fingers location on the stator, two parametric studies with varying contact angle have been conducted with Fourier analysis by using MATLAB. As a result, the significant changes of displacement strength and in-plane bending deformation angle of the protrusion fingertips were found at contact angle 30° . Hence, the piezoelectric rotary motor with cyclic symmetric stator was built for this experiment (Figure 27). The protrusion fingertips with contact angle 30° was employed in this experiment model.

The moveable base was clamped on the table with C-clamps. The stator was axis-symmetric clamped at inner radius γ_i with base by a bolt screw. In order to conduct the optimal piezoelectric ceramic buzzers mounting positions and make sure the correct structure response is obtained, the colored sand was used to visualize the Chlandi figure as shown in Figure 28. As a result, the piezoelectric ceramic buzzers are accurately placed on the positions beneath cyclic symmetric stator. The resonance frequencies were found at 1776Hz and 1778Hz in the simulation respectively. However, the experimental resonance frequencies were obtained at around 1711Hz and 1715Hz respectively. The experimental resonance frequencies are slightly different from the simulated one. It might due to the material properties and geometric parameters setting deviations. With this experimental setup, the rotation speed and direction of the spherical rotor was examined. The result shows that the rotation speed was obtained at 3.52 rpm in clockwise with diagonal angle as shown in Figure 29 when the piezoelectric ceramic buzzers were driven at $20 V_{p-p}$ with the sinusoidal wave at 1711Hz. Another result indicates that the spherical rotor remained still when the piezoelectric ceramic buzzers were driven at 1715Hz. In this experiment, the preload is applied by weight of the spherical ball rotor (2.7 grams).

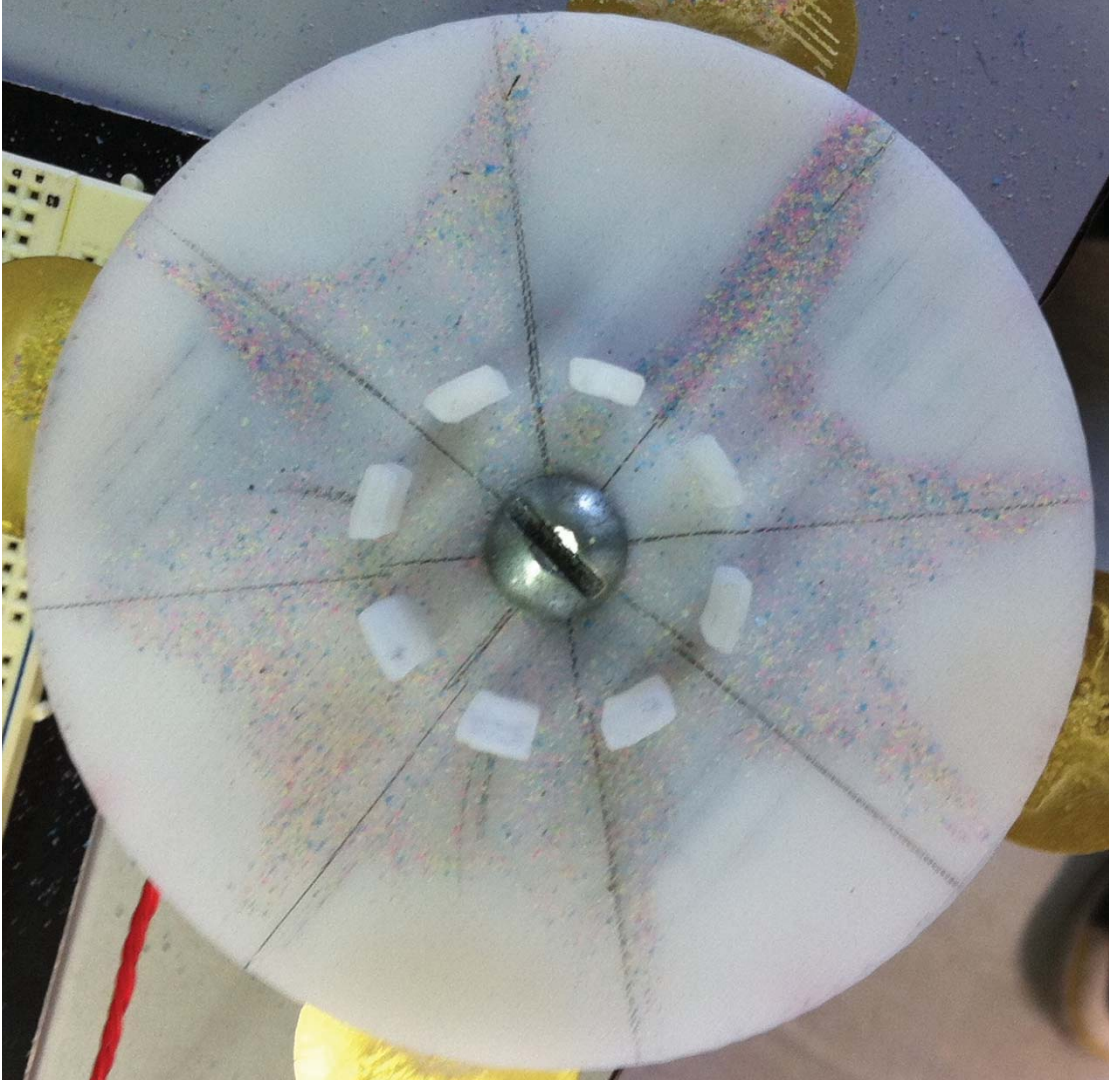


Figure 28: Chlandi-type measurement used on the cyclic symmetric stator

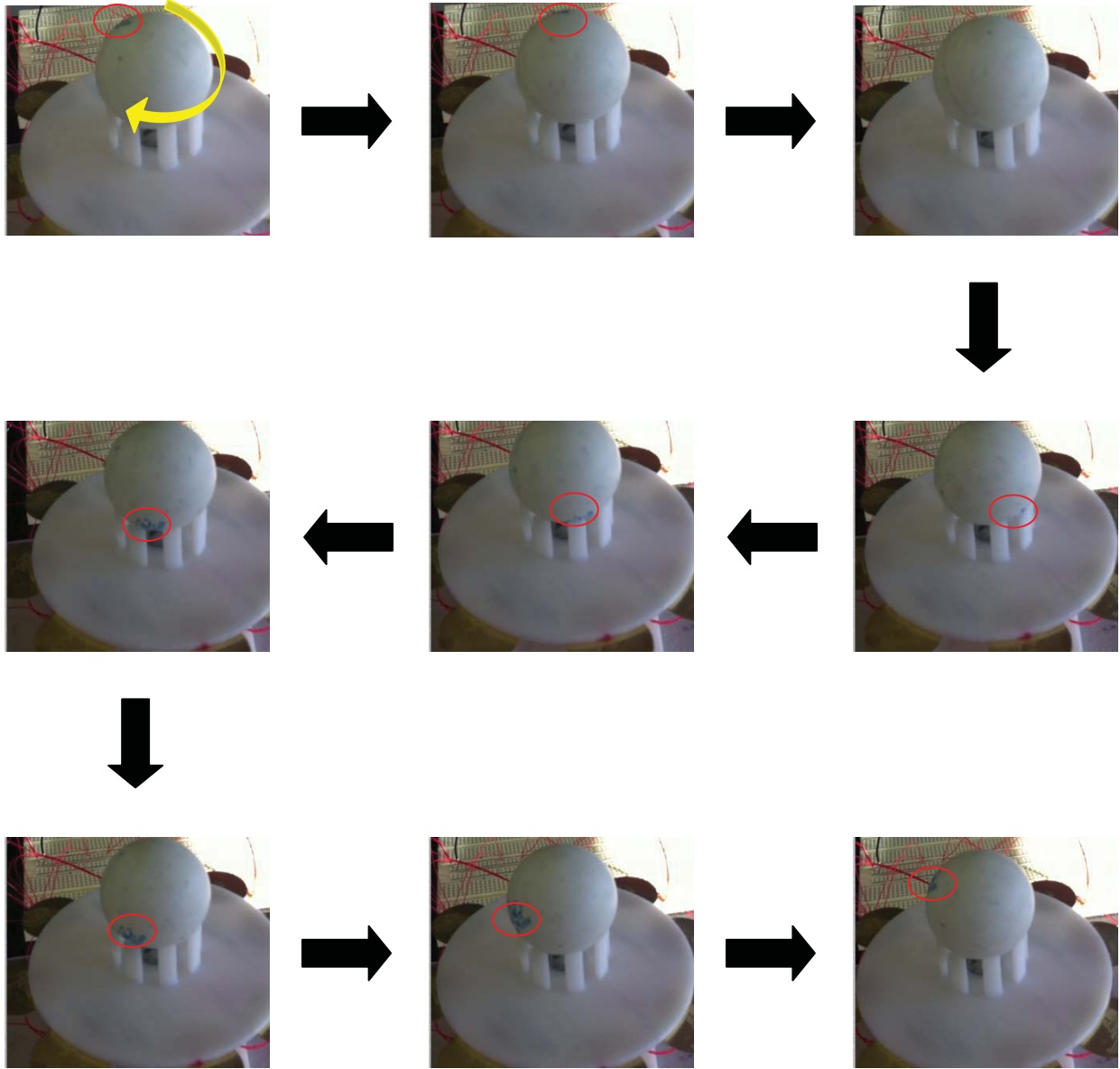


Figure 29: Rotation performance

5.3. Chapter summary

The piezoelectric rotary motor with cyclic symmetric stator driven by piezoelectric ceramic buzzers has been developed. Based on the simulated results, the optimal performance can be obtained with stator and rotor contact angle at 30° . Furthermore, the protrusion fingertips were showing the tendency of driving rotor in clockwise and diagonal direction. With this experimental setup, rotational results were obtained at rotating speed of 3.52 rpm clockwise with the diagonal angle. This result shows that the experimental model and simulated assumption match consistently.

Chapter 6

Summary

This thesis discusses the cyclic symmetric stator model in (a) relations between number of the protrusion finger design and structure response under different excitation frequencies and (b) displacement strength and in-plane bending deformation angle with varying contact angle. The following sections summarize the contributions of this thesis and provide directions for future work.

6.1. Structure response in a novel cyclic symmetric stator model

The novel piezoelectric rotary motor and cyclic symmetric stator structure was built. The frequencies and structure responses of cyclic symmetric stator with evenly-spaced protrusion fingers were discussed in Chapter 3 by using finite element simulation. The distorted motions of the stator disk and protrusion fingers were observed in different modes. The structure responses of the sine and cosine components of cyclic symmetric stator were normally repeated in different frequencies. Nevertheless, the particular split modes were found when the protrusion fingers array matched the nodal diameters. It is indicated that protrusion fingers' number significantly associated with the nodal diameters, which means the deformation behavior of the fingers can be altered by changing the design of the finger numbers. This novel finding develops a new stator design concept for piezoelectric or ultrasonic application.

6.2. Displacement strength and in-plane deformation angle of the cyclic symmetric stator

The displacement strength variation of the cyclic symmetric stator in different contact angle is discussed in chapter 4, with the emphasis placed on the strength difference between each finger. In principle, the bending motion is offset by the symmetric and opposite fingers as shown in the simulation. However, through observation and Fourier analysis, different displacement strength on the protrusion fingers was found in the different contact angle especially in 30° , this result in various rotor rotational directions. Additionally, the in-plane bending deformation angle of the protrusion fingertips is also discussed in chapter 4. The focus is placed on the bending angle rather than the bending amplitude. According to the observation, different bending deformation angle exhibited on each protrusion fingertips. These slight changes in bending deformation angle exhibited the tendency of varying rotor rotational direction. Based on these two reasons, the contact angle between stator and rotor is shown to be a design option to modify these two parameters of the fingertips for motion direction control.

6.3. Limitations

The thesis-based research contains several limitations due to the shortage of the resources. The following issues for the novel stator design with evenly-space protrusion fingers have been identified in this study.

1. Piezoelectric ceramic driving system – In this experimental prototype, the function generator and power amplifier circuit were employed as the driving sources. With this setting, the low voltage sinusoidal wave ($V_{p-p}=20V$) was employed instead of using high voltage to drive the piezoelectric actuators, which is due to the lack of the equipment. In order to fulfill the optimal actuation, plural buzzers were employed to achieve this purpose. However, it changed the mass

property and it was likely to affect the structure responses. Moreover, it is unlikely to obtain the optimal result without optimum actuation output. Hence, it is recommended that a driving system with high voltage power amplifier should be developed to drive the actuators.

2. The manufacturing of the stator and rotor – The rapid prototype technology is used to manufacture the cyclic symmetric stator in order to reduce time and cost consumption. Instead of manufacturing proper rotor, a ping-pong ball was simply used as a rotor due to technical difficulty of manufacturing a spherical-shape ball. There are some deviations exhibiting between the stator and the rotor. As a result, it is more likely to affect the rotational direction and also reduce the rotational speed. Therefore, it is recommended that the accurately manufactured stator and rotor should be replaced in order to solve these problems and ensure the rotation performance.

6.4. Directions for future work

The following directions are identified for future studies:

1. The frictional force between the stator and the rotor

The frictional force is an important factor for the rotation of the rotor. In this thesis, the contact angle between the stator and the rotor was used in the parametric studies. The contact area was changed when different contact angles were applied. The effect of the contact area change, which increases or decreases the frictional force between stator and rotor, was not considered in this thesis. However, as the rotor driving force is transmitted by the friction force of the protrusion fingers, the contact area (frictional force) between stator and rotor can be used as a design option to improve the rotation performance and durability of the stator [19] in future research.

2. The protrusion fingertip design

The protrusion fingertip was designed as arch shape. From the simulated and experimental results carried out in this thesis, each fingertip exhibited slightly difference in terms of displacement and bending angles, which affects the motion of the rotor. Hence, different fingertip design (such as shape, thickness and wideness of the fingertip) can be further employed for obtaining driving and bending force.

3. Piezoelectric ceramic actuator driving method

Another potential future research topic can be developing a new driving method to alter the finger deformed behavior. From experimental and simulated results in this study, the excitation frequencies have significantly influenced the deformations of the fingertips; therefore, multi mode can be employed at same time to affect the deformed direction of the fingertips.

Reference

1. Sashida, T., & Kenjo, T. (1993). *Introduction to Ultrasonic Motors*. New York, N.Y.: Oxford University Press.
2. Ueha, S., Tomikawa, Y., Kurosawa, M., & Nakamura, N. (1993). *Ultrasonic Motors: Theory and Applications*. New York, N.Y.: Clarendon Press.
3. Flynn, A. M., Tavrow, L. S., Bart, S. F., Brooks, R. A., Ehrlich, D. J., Udayakumar, K. R., & Cross, L. E. (1992). Piezoelectric micromotors for microrobots. *Journal of Microelectromechanical Systems*, 1(1). doi:10.1109/84.128055
4. Barth, H. V. (1973). Ultrasonic driven motors. *IBM Technical Disclosure Bulletin*, 16(7), 2236.
5. Lavrinenko, V. V., Vishnevski, S. S., & Kartashev, I. K. (1976). Izvestiya vysshikh uchebnykh zavedenii. *Radioelektronika.*, 13(57).
6. Vasiliev, P. E., Klimavichjus, P.-A. R., Kondratiev, A. V., Matsjukyavichjus, J. J., Gabrieljus-Vitautas, Beksha, L., & Kaminskas, V. A. (1979). *UK Patent Application. GB2020857 UK*.
7. Kumada, A. (1985). A piezoelectric ultrasonic motor. *Japanese Journal of Applied Physics*, 24, Suppl. 24-2 739-741.
8. Iwamatsu, S., Ueha, S., Kuribayashi, M., & Mori, E. (1985). Rotary ultrasonic motor using extensional vibration of a ring. *Japanese Journal of Applied Physics*, 25, Suppl. 25-1 174-176.
9. Kurosawa, M., Nakamura, K., Okamoto, T., & Ueha, S. (1989). An ultrasonic motor using bending vibrations of a short cylinder. *IEEE Transactions on*

Ultrasonics, Ferroelectrics and Frequency Control, 36(5), 517-521.
doi:10.1109/58.31795

10. Toyoda, J., & Murano, K. (1991). A small-size ultrasonic linear motor. *Japanese Journal of Applied Physics*, 30, 2274-2276. doi:10.1143/JJAP.30.2274
11. Aoyagi, M., Satoh, A., & Tomikawa, Y. (1992, August). *High torque ultrasonic motor using longitudinal and torsional vibrations*. presented at the meeting of the Proceedings of the Eighth IEEE International Symposium on Applications of Ferroelectrics., Greenville, SC , USA doi:10.1109/ISAF.1992.300571
12. Kawano, H., Ando, H., Hirahara, T., Yun, C., & Ueha, S. (2005). Application of a multi-DOF ultrasonic servomotor in an auditory tele-existence robot. *IEEE Transactions on Robotics*, 21(5), 790-800. doi:10.1109/TRO.2005.851372
13. Takemura, K., Park, S., & Maeno, T. (2008). Control of multi-DOF ultrasonic actuator for dexterous surgical instrument. *Journal of Sound and Vibration*, 311(3-5), 652-666.
14. Toyama, S., Zhang, G., Sugitani, S., Hasegawa, S., Nakamura, K., & Miyatani, Y. (1995). Development of an actuator for a robotic manipulator with ultrasonic motor: 2nd development of prototypal spherical ultrasonic motor. *Journal of the Robotics Society of Japan*, 13(2), 235-241.
15. Takemura, K., Kojima, N., & Maeno, T. (1998, August). *Development of a bar-shaped ultrasonic motor for three degrees-of-freedom motion*. presented at the meeting of the Proceedings of the Fourth International Conference on Motion and Vibration Control, Zurich, Swizerland.
16. Yun, C.-H., Niwano, S., Friend, J. R., Nakamura, K., & Ueha, S. (2003). Support mechanism for the ball rotor in the three-degree-of-freedom ultrasonic motor. *Japanese Journal of Applied Physics*, 42, 3000-3001.

17. Chang, J. Y., & Wickert, J. A. (2001). Response of modulated doublet modes to travelling wave excitation. *Journal of Sound and Vibration*, 242(1), 69-83. doi:10.1006/jsvi.2000.3363
18. Shen, I. Y. (1994). Vibration of rotationally periodic structures. *Journal of Sound and Vibration*, 172(4), 459-470.
19. Ferreira, A., & Fontaine, J.-G. (2003). Dynamic modeling and control of a conveyance microrobotic system using active friction drive. *IEEE/ASME Transactions on Mechatronics*, 8(2), 188-202. doi:10.1109/TMECH.2003.812822

Appendix

A1. MATLAB Code

Disk edge displacement with corresponding Fourier coefficients

```
clear all

%A=Degree (0 15 30 45 60)
A=45;
%T=Sine 1, Cosine 2
T=2;
H=10;

X=load(['Disk_x' '_' num2str(A) num2str(T) '.txt']);
Y=load(['Disk_y' '_' num2str(A) num2str(T) '.txt']);
Z=load(['Disk_z' '_' num2str(A) num2str(T) '.txt']);

%R=X(:,2);
R=Y(:,2);
%R=Z(:,2);
%R=sqrt(X(:,2).^2+Y(:,2).^2+Z(:,2).^2);

temp=size(R);

for i=0:temp-1
    q(i+1,1)=i*2*pi/temp(1,1);
end

figure
```

```

subplot(211)
plot(q*360/2/pi,R)
XLIM([0 360])
set(gca,'XTick',[0 90 180 270 360])
%ylim([-20000 20000])
xlabel('\theta, degree')
ylabel('Radial displacement, mm')

subplot(212)
test=ProfileDFT(R,H,0);
bar(test(:,1),test(:,2:4));
axis normal
xlabel('Harmonics, h')
ylabel('Amplitude')
Legend('Cosine - A_h', 'Sine - B_h', 'Magnitude - C_h')

```

Finger bottom edge displacement with corresponding Fourier coefficients

```

clear all

%A=Degree (0 15 30 45 60)
A=45;
%T=Sine 1, Cosine 2
T=2;
H=10;
X=load(['FB_x' '_' num2str(A) num2str(T) '.txt']);
Y=load(['FB_y' '_' num2str(A) num2str(T) '.txt']);
Z=load(['FB_z' '_' num2str(A) num2str(T) '.txt']);

%R=X(:,2);
R=Y(:,2);

```

```

%R=Z(:,2);
%R=sqrt(X(:,2).^2+Y(:,2).^2+Z(:,2).^2);

temp=size(R);

for i=0:temp-1
    q(i+1,1)=i*2*pi/temp(1,1);
end

figure
subplot(211)
plot(q*360/2/pi,R)
XLIM([0 360])
set(gca,'XTick',[0 90 180 270 360])
%ylim([-20000 20000])
xlabel('\theta, degree')
ylabel('Radial displacement, mm')

subplot(212)
test=ProfileDFT(R,H,0);
bar(test(:,1),test(:,2:4));
axis normal
xlabel('Harmonics, h')
ylabel('Amplitude')
Legend('Cosine - A_h', 'Sine - B_h', 'Magnitude - C_h')

```

ProfileDFT for Fourier data(harmonic calculation)

```

function DFT=ProfileDFT(data,H,flag)
SID=length(data);
x=0:(SID-1);

```

```

stopH=H;

if flag == 0
    startH=0;Fourierdata=zeros(H+1,4);
else
    startH=stopH;Fourierdata=zeros(1,4);
end

for k=startH:stopH
    f1i=data.*cos(k*2*pi.*(x')/SID);
    f2i=data.*sin(k*2*pi.*(x')/SID);

    if flag == 0
        if k == 0
            ai(k+1,1)=sum(f1i)/SID;
        else
            ai(k+1,1)=sum(f1i)/SID*2;
        end
        bi(k+1,1)=sum(f2i)/SID*2;
        %ci(k+1,1)=sqrt(ai(k+1)^2+bi(k+1)^2);
    else
        if k == 0
            ai(1,1)=sum(f1i)/SID;
        else
            ai(1,1)=sum(f1i)/SID*2;
        end
        bi(1,1)=sum(f2i)/SID*2;
        %ci(1,1)=sqrt(ai(1)^2+bi(1)^2);
    end
end
end

```

```
Fourierdata(:,1)=(startH:stopH)';  
Fourierdata(:,2)=ai;  
Fourierdata(:,3)=bi;  
%Fourierdata(:,4)=ci;  
  
DFT=Fourierdata;
```

A2. MATLAB Figure

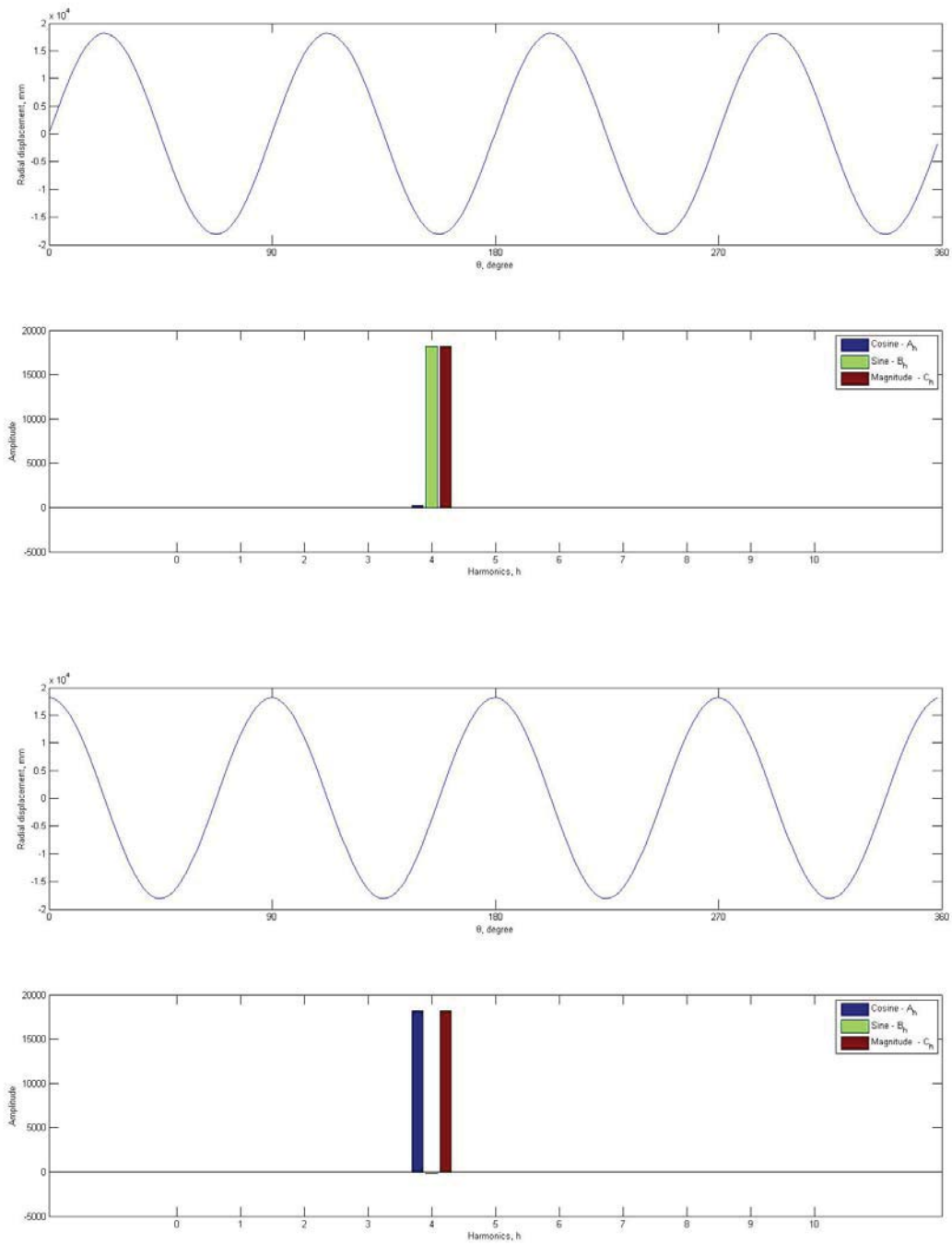


Figure 30: 0° disk edge displacement and corresponding harmonic

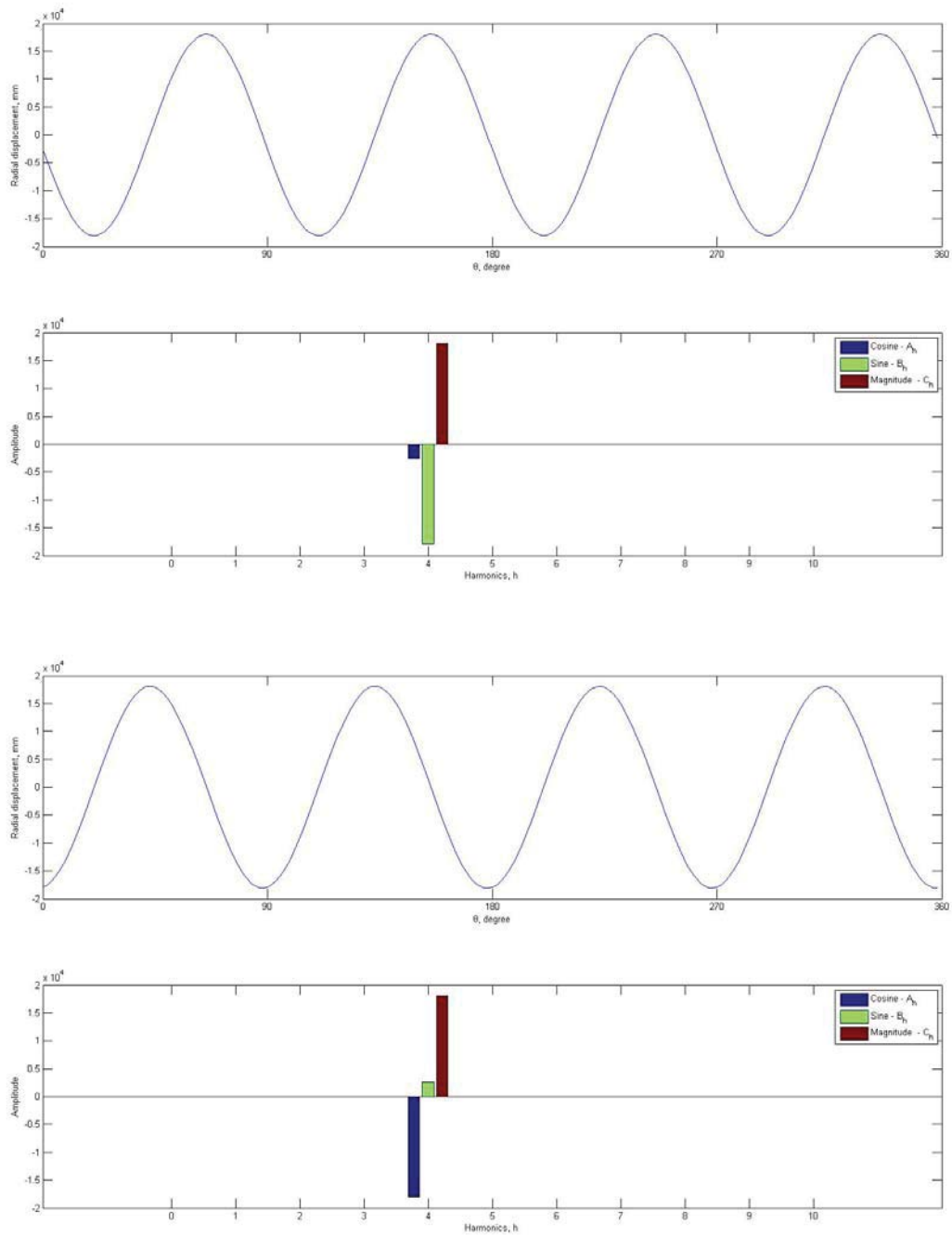


Figure 31: 15° disk edge displacement and corresponding harmonic

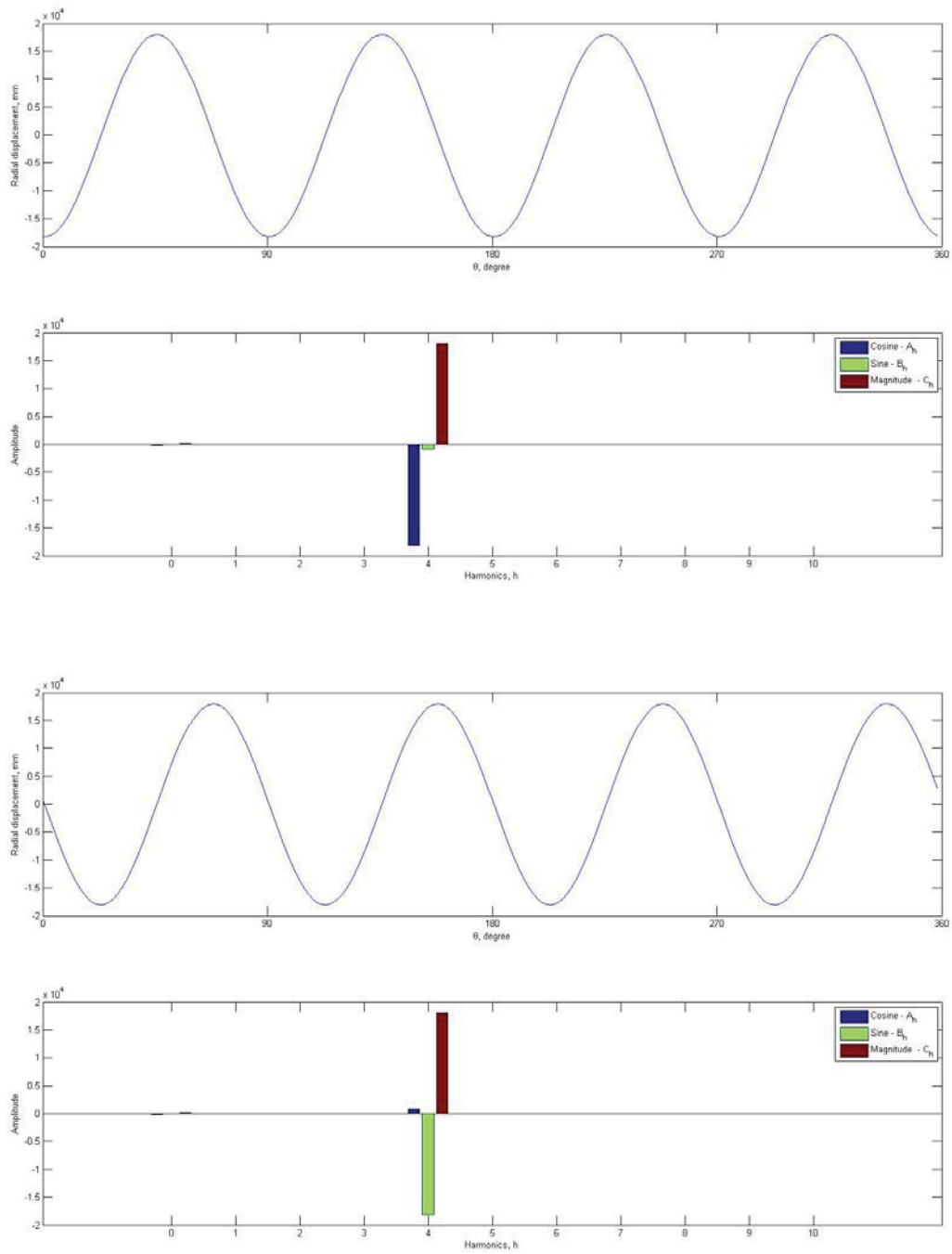


Figure 32: 30° disk edge displacement and corresponding harmonic

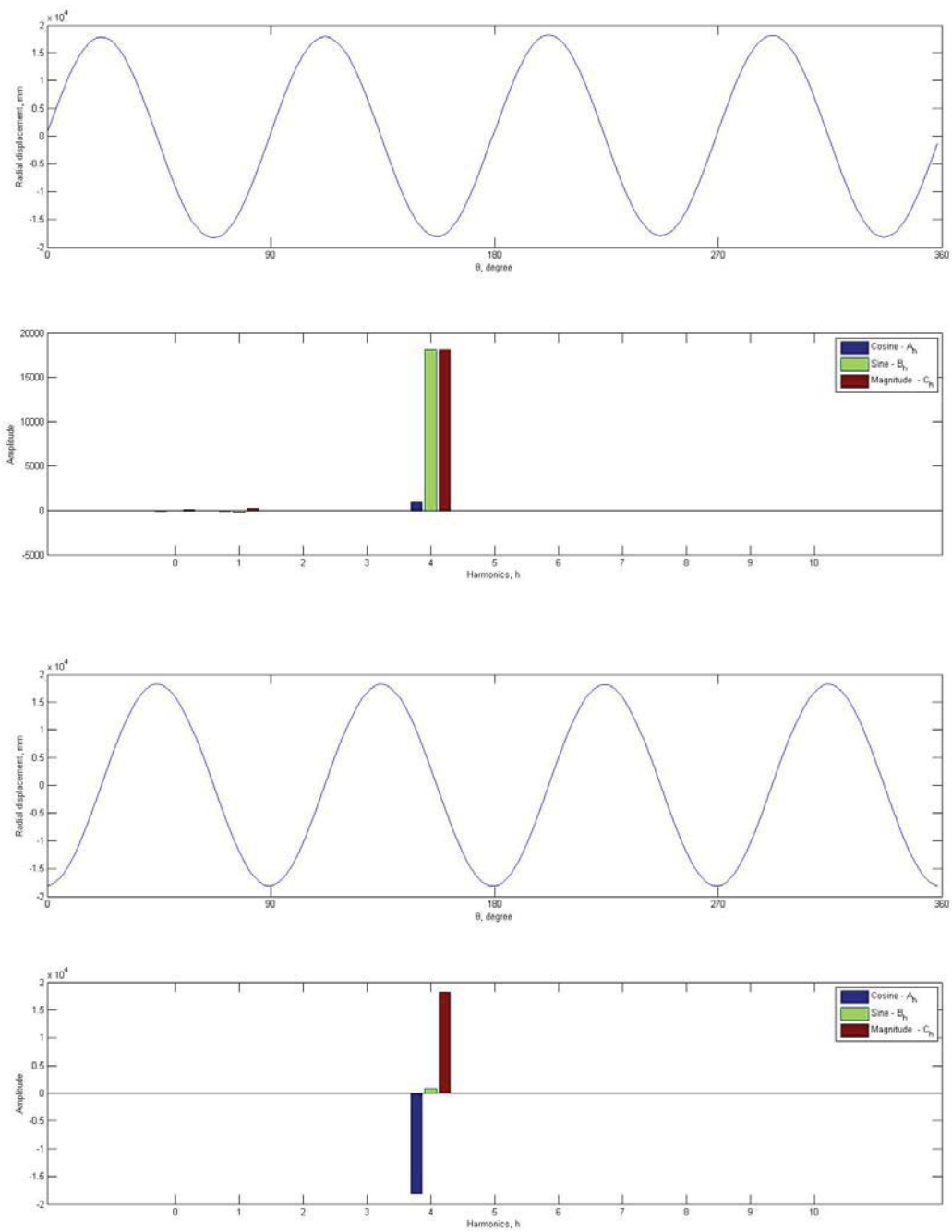


Figure 33: 45° disk edge displacement and corresponding harmonic

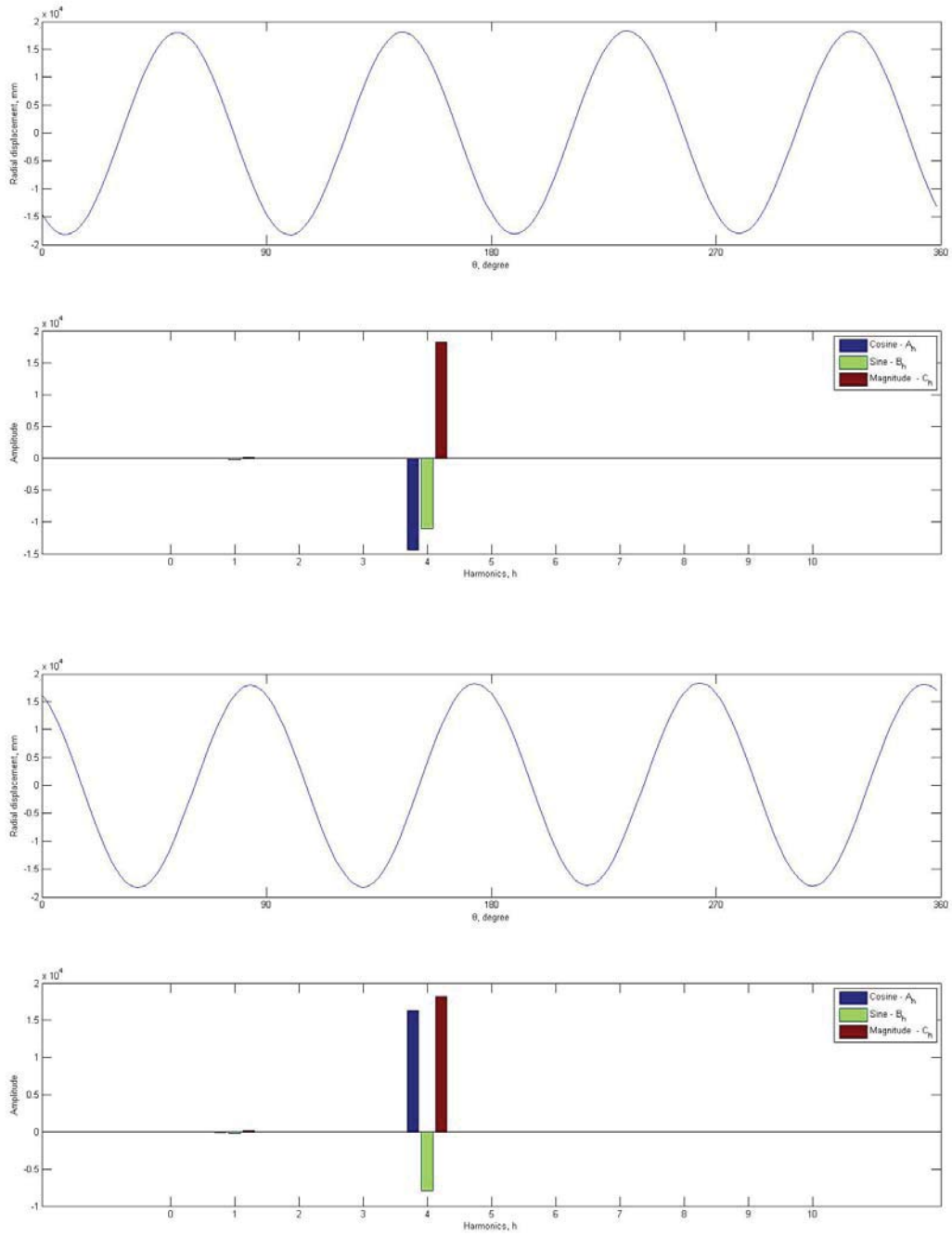


Figure 34: 60° disk edge displacement and corresponding harmonic

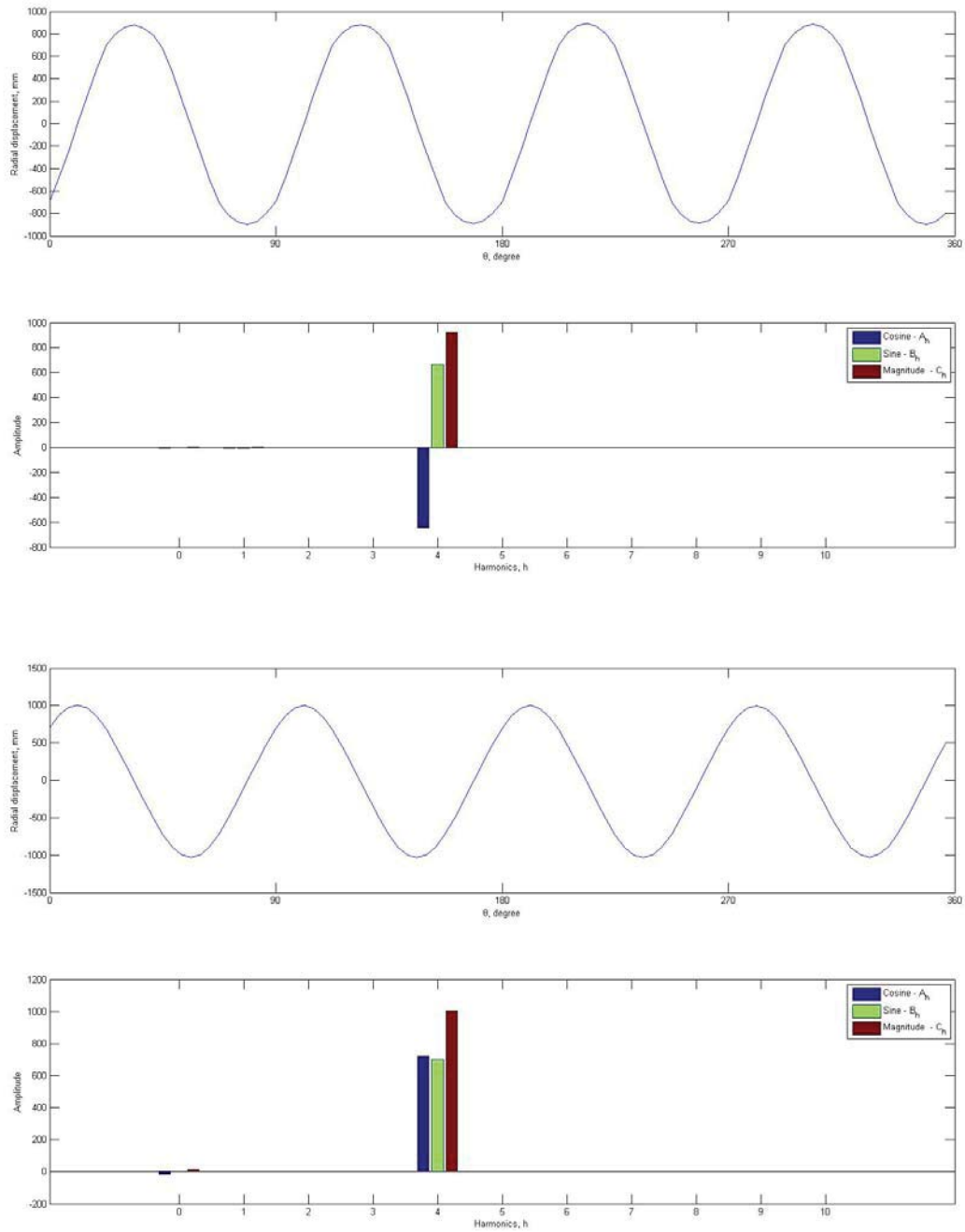


Figure 35: 0° finger base displacement and corresponding harmonic

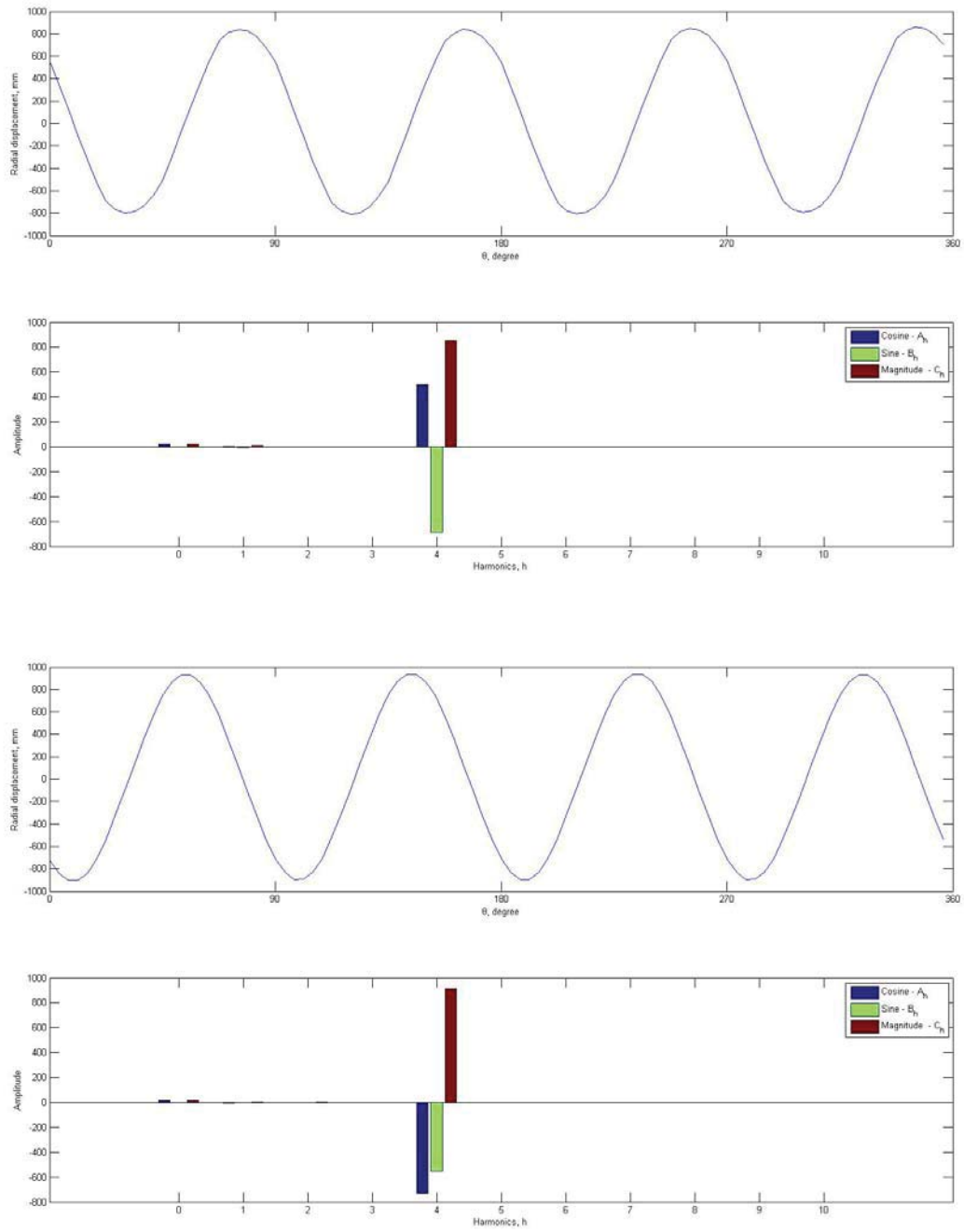


Figure 36: 15° finger base displacement and corresponding harmonic

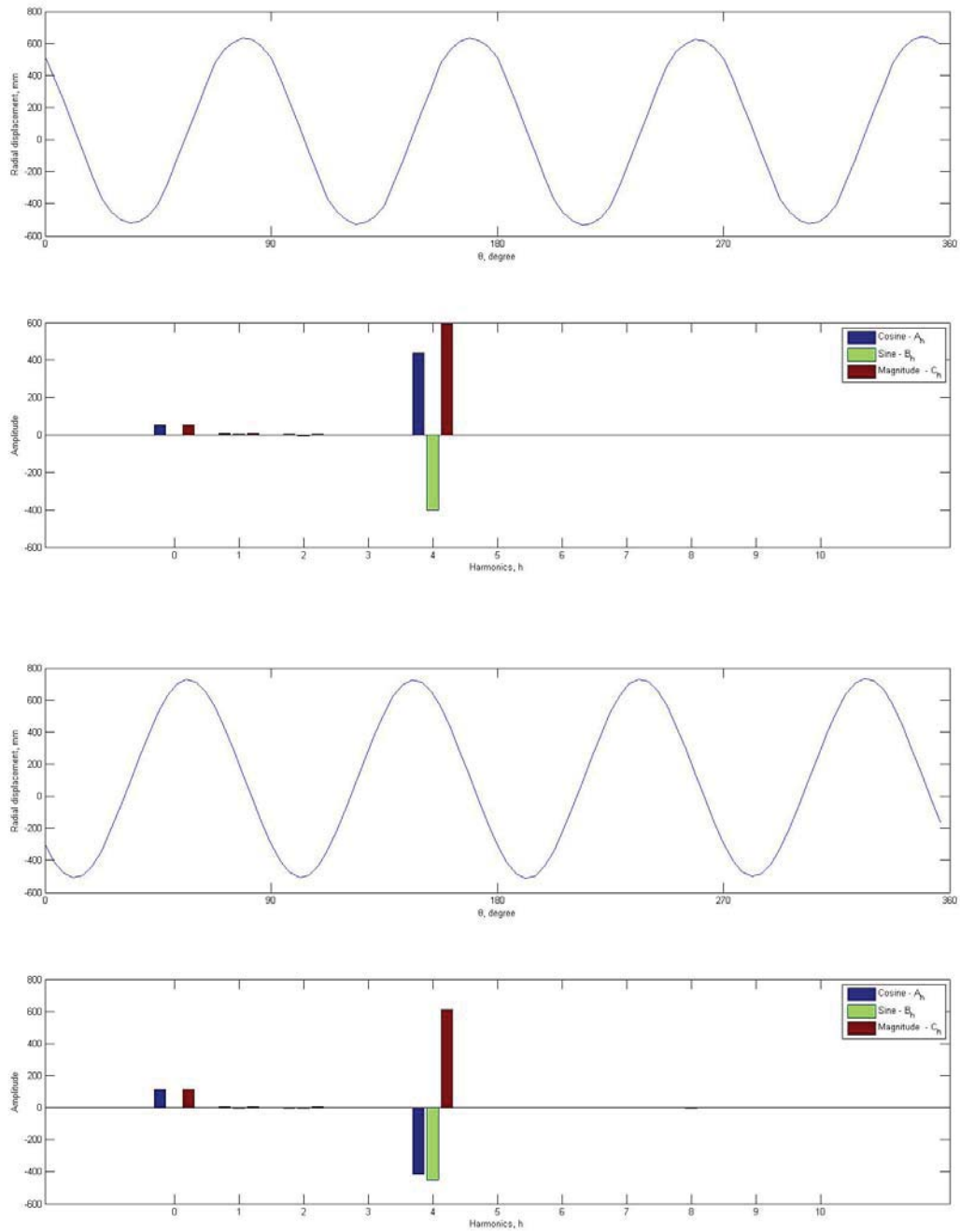


Figure 37: 30° finger base displacement and corresponding harmonic

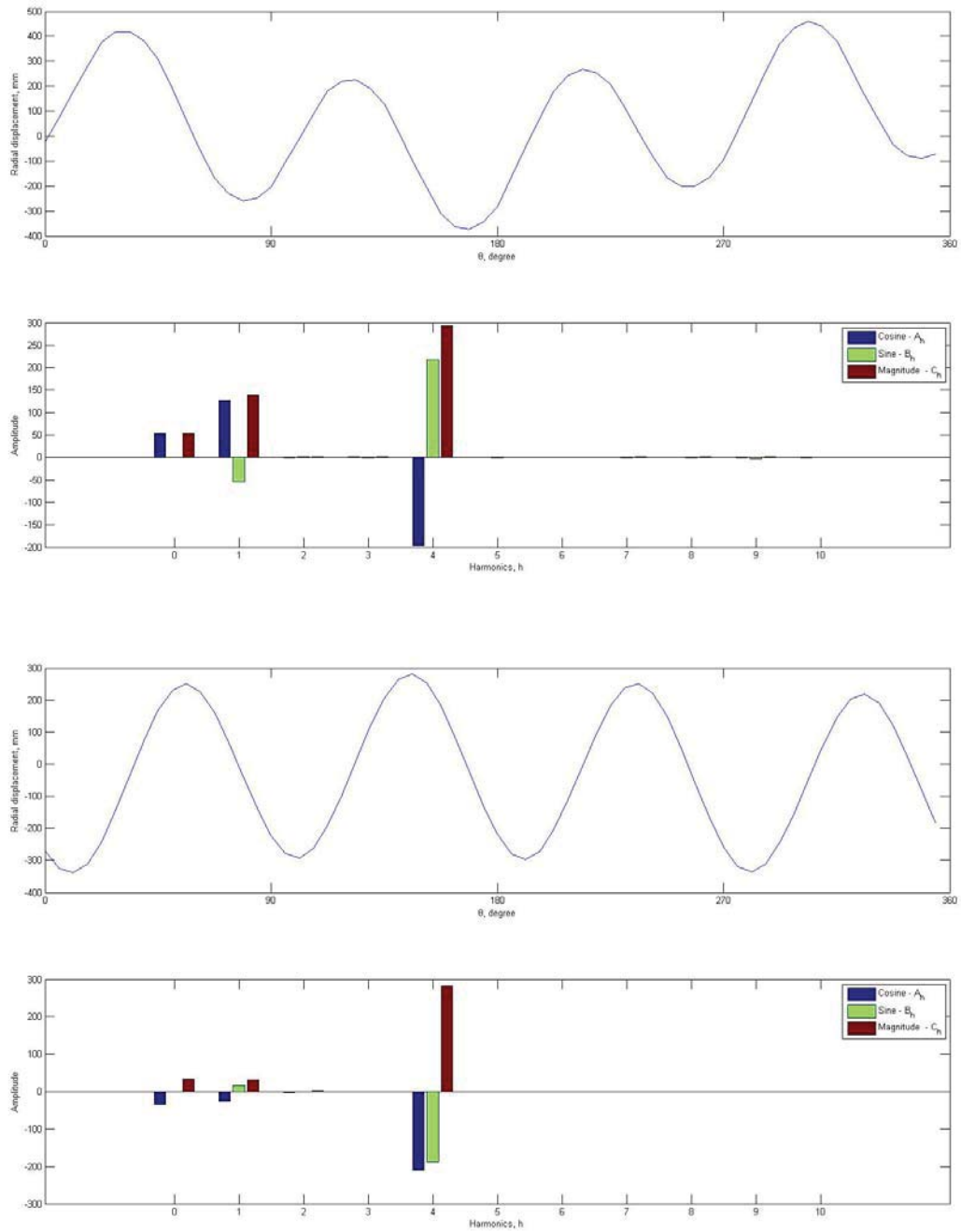


Figure 38: 45° finger base displacement and corresponding harmonic

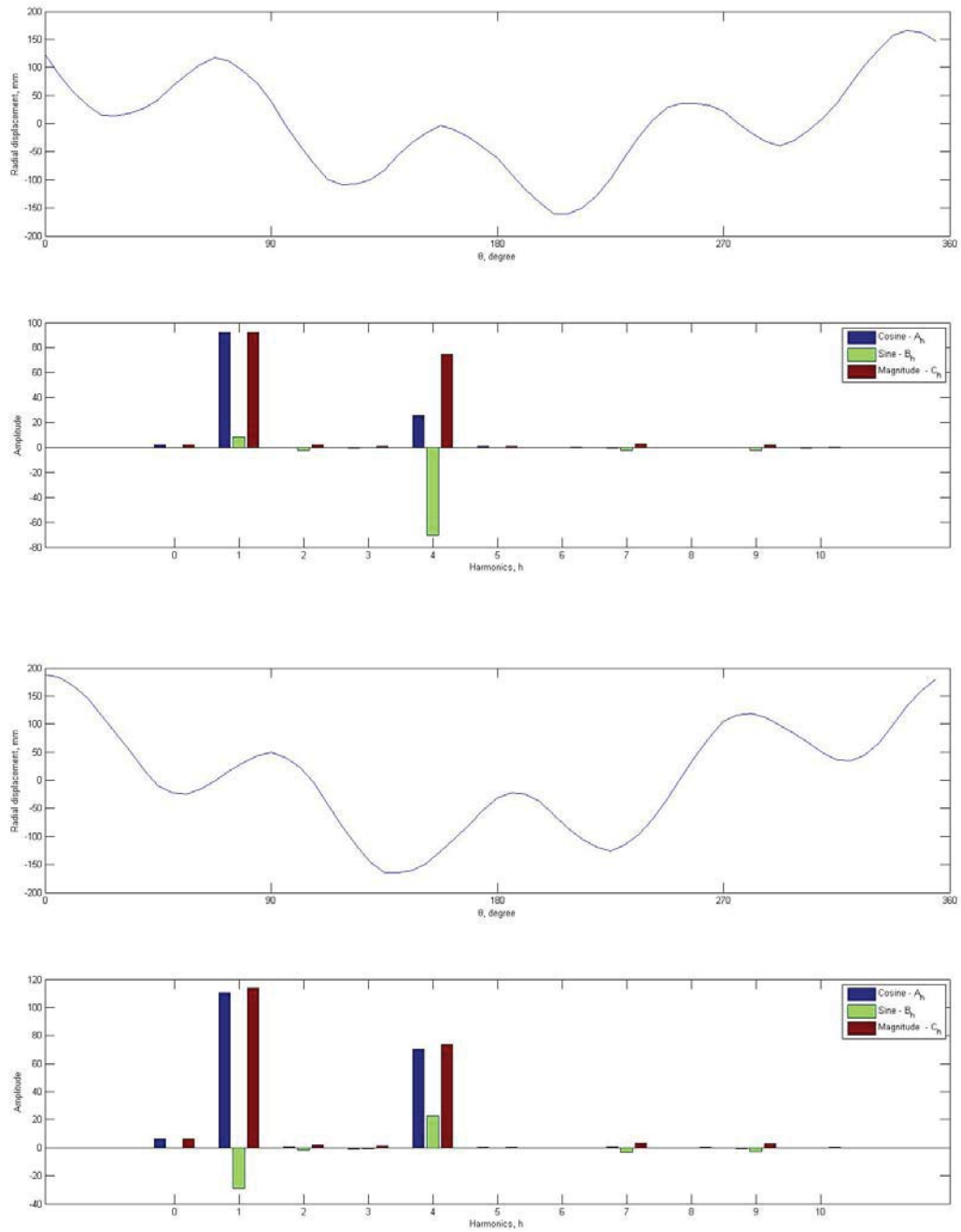


Figure 39: 60° finger base displacement and corresponding harmonic